Hydromechanical–Stochastic Modeling of Fluid-Induced Seismicity in Fractured Poroelastic Media[1]

Lei Jin

Department of Geophysics, Stanford University, California 94305

leijin@alumni.stanford.edu

Key Points

- Inter-seismic fracture-poro-mechanics combined with stochastic co-seismic stress drop for modeling fluid-induced seismicity in fractured poroelastic media
- Mechanics-based analysis on the spatial-temporal evolution of seismicity and the associated source parameters
- Seismicity clusters near favorably-oriented large-scale fractures and substantially inhibited by poroelastic coupling in the near field

Abstract

We present a new method for modeling fluid-perturbation induced seismicity in a fluid-saturated poroelastic medium embedded with a dual network of fractures. The inter-seismic triggering is deterministically modeled using a quasi-static, nonlinear and fluid-solid fully coupled fracture-poro-mechanical approach that resolves only the large-scale fractures. The co-seismic dynamic rupture is not explicitly modeled. Instead, the seismicity-induced shear stress drop is approximated as a static quantity and stochastically modeled on a range computed from the evolving poroelastic stress in conjunction with the initial stress and the static and dynamic frictional strengths. These two steps are sequentially connected and then iterated via a prediction-correction type of fracture stress updating scheme, naturally producing repeating seismic events on certain fractures. As an example, we perform three progressive numerical experiments. By comparing the corresponding synthetic event catalogs, we investigate the effects of fractures and poroelastic coupling on the evolution and source characteristics of the seismicity. Main findings include (1) the seismicity clusters near large-scale fractures favorably oriented and subjected to sufficient perturbations, (2) poroelastic coupling enhances the clustering and substantially inhibits the seismicity in the nearfield and (3) source characteristics and the b-value seem not affected by fractures or poroelastic coupling. Our method can serve as a general physics-based tool for more realistically predicting induced seismicity in complex geological media.

---

[1] This article is a non-peer reviewed preprint published at EarthArXiv.

31 **Keywords**: numerical modeling, induced seismicity, discrete fracture network, poroelastic
32 coupling, stress drop, *b*-value

33 1. Introduction

34 Fluid injection into the subsurface perturbs the pore pressure and alters the effective stress quasi-
35 statically, inducing seismicity on fractures of certain orientations (we hereinafter do not
36 distinguish between a fracture and a fault in this study). This process is traditionally considered
37 as a decoupled hydroshear process: the effective normal stress on a fracture decreases by the
38 amount of fluid overpressure according to the simple effective stress law (Terzaghi, 1936),
39 whereas the shear stress remains unchanged (e.g., Byerlee, 1978; Scuderi & Collettini, 2016;
40 Mukuhira et al, 2017), resulting in a direct increase in the Coulomb stress, which, when driven
41 from negative to zero, signifies the occurrence of seismicity. Such a decoupled mechanism
42 remains as the basis of some prevalent statistical models of induced seismicity in a permeable
43 porous medium (e.g., Shapiro et al., 2005; Rothert & Shapiro, 2007). In this class of models, a
44 statistically random critical pore pressure is used as a proxy of the frictional strength of a pre-
45 existing fracture and the pore pressure evolution is governed by simple linear fluid diffusion; the
46 modeled spatial-temporal distribution of seismicity, however, is often inconsistent with
47 observations. As a remedy, some nonlinear diffusion models have been developed by adding a
48 pressure-dependent diffusivity (Hummel & Shapiro, 2012; Johann et al., 2016; Carcione et al.,
49 2018). The diffusion-based seismicity models can be further extended by incorporating, e.g.,
50 random stress heterogeneity (Goertz-Allmann & Wiemer, 2012), fractures following distributions
51 derived from field observations (Verdon et al., 2015), and even empirical seismic emission criteria
52 for generating synthetic seismograms (Carcione et al., 2015). This decoupled mechanism also
53 underlies some studies that invert for distributions of permeability (Tarrahi & Jafarpour, 2012)
54 and pore pressure (Terakawa et al., 2012; Terakawa, 2014) from induced seismicity data.

55 However, the decoupled mechanism inherently cannot explain the remoting triggering of
56 seismicity in areas not subjected to pressure perturbation (Stark & Davis, 1996; Megies &
57 Wassermann, 2014; Yeck et al., 2016); it also directly contradicts the commonly observed
58 depletion-induced seismicity (Zoback & Zinke, 2002). Motivated by such field evidences, a large
59 body of analytical solutions (Segall, 1985; Segall et al., 1994; Segall & Fitzgerald, 1998; Altmann et
60 al., 2014; Segall & Lu, 2015; Jin & Zoback, 2015a) and numerical solutions (Murphy et al., 2013;
61 Chang & Segall, 2016a; Chang & Segall, 2016b; Chang & Segall, 2017; Fan et al., 2016; Deng et al.,
62 2016; Zbinden et al., 2017) have been proposed, providing poroelastic models of induced
63 seismicity. At a smaller scale, numerical simulations of fluid-induced microseismicity, typically
64 motivated by applications to the stimulation of hydrocarbon and geothermal reservoirs, have also
65 been reported (e.g., Maillot et al., 1999; Baisch et al., 2010; Wassing et al., 2014; Zhao & Young,
66 2011; Yoon et al., 2014; Raziperchikolaee et al., 2014; Riffracture et al., 2016). Irrespective of the

67 scale of interest, these studies substantiate that poroelastic coupling may play an important role
68 in inducing seismicity.

69 Despite these evidences, some debates persist, mainly from those who advocate the simple
70 diffusion-only models (Johann et al., 2016). They claim that their diffusion models approximate
71 poroelastic models if the Biot-Willis coefficient a is small; they also argue that when a is less than
72 0.3, it is the pore pressure rather than the poroelastic stress that dominates the hydroshear on
73 fractures; they further question the Segall (2015, 2016a) poroelastic models in which a is greater
74 than 0.3, and hypothesize that for nearly impermeable rocks, a should also be negligible.
75 However, one must realize that a is a measurement of the rock solid's susceptibility to the
76 influence of the fluid and vice versa; it is not a property directly related to the permeability of the
77 rock itself. As a matter of fact, laboratory experiments show that a of unconventional reservoir
78 rocks is indeed primarily between 0.3 and 0.9 (e.g., Ma & Zoback, 2017).

79 Some other studies seek middle ground by considering the co-existence of the pore pressure effect
80 and the poroelatic effect such that induced seismicity is a result of both (e.g., Barbour et al., 2017;
81 Keranen & Weingarten, 2018). This is perhaps a misconception. Jin & Zoback (2017) demonstrated
82 the fundamental difference between the two, which lies in how the fluid overpressure modifies
83 the effective stress tensor that will be used for calculating stress on a fracture. Using the Biot
84 effective stress law (Biot, 1941) as an example, the pore pressure effect is stated as:

$$\boldsymbol{\sigma}_p{}' + \alpha\, p\mathbf{1} = \mathbf{0} \tag{1}$$

86 whereas the poroelastic effect, more precisely, the fluid-to-solid coupling effect, arise from
87 solving the following conservation law:

$$\nabla \cdot \left(\boldsymbol{\sigma}_p{}' + \alpha\, p\mathbf{1}\right) = 0 \tag{2}$$

89 Here in equations (1) and (2), p is the fluid overpressure, $\boldsymbol{\sigma}_p'$ is the associated change in the
90 effective stress tensor (both are quasi-static perturbations to their respective initial reference state)
91 and $\mathbf{1}$ is the Kronecker delta. $\boldsymbol{\sigma}_p'$ is the fundamental reason driving changes in the stress on a
92 fracture and inducing seismicity. Since the linear momentum should be always conserved
93 between the perturbations, one must solve for $\boldsymbol{\sigma}_p'$ from equation (2) instead of simply assuming
94 $\boldsymbol{\sigma}_p' = -ap\mathbf{1}$ as is stated by equation (1). As a matter of fact, $\boldsymbol{\sigma}_p' \neq -ap\mathbf{1}$ as long as p is not spatially
95 uniform (i.e., a pressure gradient is present, $\nabla p \neq 0$). For any fluid saturated media, the poroelastic
96 coupling effect is the true and only effect; the pore pressure effect is the 'reduced' poroelastic
97 effect when the pressure gradient vanishes and the two should not be considered as co-existing
98 effects.

99 Poroelastic coupling is undoubtedly the mechanism behind induced seismicity. However, the
100 exact role is plays and its influence on the source characteristics remain somewhat unclear.

101 Furthermore, the aforementioned poroelastic models only include fractures very limited in
102 distribution, therefore, the role of fractures cannot be sufficiently explored, neither. The fractures
103 are also explicitly represented as entities following the same fluid and solid rheologies as the
104 hosting rock, therefore, the medium is effectively 'porous' only. Such simplifications may come
105 with certain consequences. Some studies suggest that accounting for both poroelastic coupling
106 and an arbitrary discrete fracture network (DFN) permitted to have different constitutive
107 behaviors can lead to radically different modeling outcomes (Jin & Zoback, 2016a; Jin & Zoback,
108 2016b). Pertaining to this issue, some studies resolve very regularly distributed fractures (e.g.,
109 Safari & Ghassemi, 2016); others attempt to include an arbitrary DFN, among which, e.g., some
110 focus on the fluid pressure and solid deformation only within fractures but not the hosting rock
111 (Farmahini-Farahani & Ghassemi, 2016), some consider coupling only upon the occurrence of
112 seismicity (Bruel, 2007). None of these models produces repeating events frequently detected in
113 catalogs of induced seismicity (e.g., Baisch & Harjes, 2003; Moriya et al., 2003; Deichmann et al.,
114 2014; Duverger et al, 2015).

115 To date, a general method for modeling fluid-induced seismicity accounting for arbitrary
116 fractures and poroelastic coupling is lacking. We are therefore motivated to develop the following
117 new method aimed for a fractured poroelastic medium. It combines the deterministic modeling
118 of inter-seismic, quasi-static and hydromechanically coupled triggering and the stochastic
119 modeling of co-seismic shear stress drop, both repeated over multiple seismic cycles. It is capable
120 of not only realistically predicting the spatial-temporal evolution of seismicity but also generating
121 a synthetic event catalog that allows for the exploration of the role of model physics as well as
122 their connections to observations. Details are described below.

2. Methodology

2.1 Sources of Fracture Stress

125 Given a location $\underline{x}$ and a time t over $\Omega \times [0, T]$ where Ω is the domain of interest and $[0, T]$ is the
126 time interval, the effective stress tensor $\boldsymbol{\sigma}'(\underline{x}, t)$ in a fluid-saturated poroelastic medium
127 undergoing seismicity can be decomposed as the following:

$$\boldsymbol{\sigma}'(\underline{x},t) = \boldsymbol{\sigma}_0'(\underline{x}) + \boldsymbol{\sigma}_p'(\underline{x},t) + \sum_j \boldsymbol{\sigma}_s'(\underline{x}, t_j^* + \delta t_j) \tag{3}$$

129 where $\boldsymbol{\sigma}_0'(\underline{x})$ is the initial in-situ effective stress tensor, $\boldsymbol{\sigma}_p'(\underline{x}, t)$ is the fluid perturbation-induced
130 effective stress tensor relative to $\boldsymbol{\sigma}_0'(\underline{x})$ (same as in equation (1) and (2)) and $\boldsymbol{\sigma}_s'(\underline{x}, t_j^* + \delta t_j)$ is the slip-
131 induced change in the effective stress tensor over the jth co-seismic interval where t_j^* and δt_j are
132 the associated beginning time and duration. $\boldsymbol{\sigma}_0'(\underline{x})$ is time-independent and in principle permits
133 heterogeneity; $tr(\boldsymbol{\sigma}_p'(\underline{x}, t))$ (the diagonal sum) is fully coupled with the negative gradient of the
134 associated fluid pressure $p(\underline{x},t)$ and the two must be solved for simultaneously; in $\boldsymbol{\sigma}_s'(\underline{x}, t_j^* + \delta t_j)$,

135 $\delta t_j \ll t$ such that relative to the time scale relevant to a complete seismic cycle, $\delta t_j \approx 0$ and $\sigma_s'(\underline{x}, t_j^* + \delta t_j)$
136 can be approximated as a static quantity:

$$\sigma_s'(\underline{x}, t_j^* + \delta t_j) \approx \sigma_{sj}'(\underline{x}) \tag{4}$$

138 The stress on a fracture intersecting $\underline{x}$ and at t is given by:

$$\sigma_n'(\underline{x}, t) = \sigma'(\underline{x}, t) : \underline{n} \otimes \underline{n} \tag{5}$$

$$\tau(\underline{x}, t) = \left[\left\| \sigma'(\underline{x}, t) \cdot \underline{n} \right\|^2 - \left(\sigma'(\underline{x}, t) : \underline{n} \otimes \underline{n} \right)^2 \right]^{\frac{1}{2}} \tag{6}$$

$$CFF(\underline{x}, t) = \tau(\underline{x}, t) - \mu_s \sigma_n'(\underline{x}, t) \tag{7}$$

142 In equations (5) - (7), $\sigma_n'(\underline{x}, t)$, $\tau(\underline{x}, t)$ and $CFF(\underline{x}, t)$ are the effective normal stress, the shear stress
143 and the Coulomb Failure Function (i.e., the Coulomb stress, ≤ 0) on the fracture of interest, and
144 $\underline{n}$ and μ_s are the unit normal vector and the static frictional coefficient of the fracture.

145 Equations (3) - (7) show that $\sigma_p'(\underline{x}, t)$ and $\sigma_{sj}'(\underline{x})$ are the two primary sources driving changes in
146 the stress on a fracture. In general, for $\sigma_n'(\underline{x}, t)$, $\sigma_p'(\underline{x}, t)$ can either increase or decrease it whereas
147 $\sigma_{sj}'(\underline{x})$ causes minor variations to it except near fracture tips; for $\tau(\underline{x}, t)$, $\sigma_p'(\underline{x}, t)$ compensates, albeit
148 possibly negatively depending on the configuration, the fracture for the shear stress loss resulting
149 from $\sigma_{sj}'(\underline{x})$.

150 To model induced seismicity in a fractured poroelastic medium, one must go through equations
151 (3)-(7) and check $CFF(\underline{x}, t)$ against 0 to determine if seismicity occurs; if yes, the effective stress
152 tensor needs be updated ($j=j+1$) for the next seismic cycle. This process needs to be repeated
153 iteratively for all fractures at all time steps. For a given fracture that has undergone at least one
154 seismic cycle, equations (3)-(6) yield a complete stress path associated with this cycle in the
155 fracture effective normal stress-shear stress space. CFF remains constrained below 0 throughout
156 the process.

157 The major computational cost then arises from the calculation of $\sigma_p'(\underline{x}, t)$ over the quasi-static
158 inter-seismic (i.e., pre-seismic and post-seismic) phase and $\sigma_s'(\underline{x}, t_j^* + \delta t_j)$ (or $\sigma_{sj}'(\underline{x})$) over the co-
159 seismic phase. Notice these two quantities can be solved for separately if assuming a linearly
160 elastic solid irrespective of the fluid which can behave either linearly or nonlinearly. The former
161 can be sufficiently addressed using our Jin & Zoback (2017) computational model; for a detailed
162 description on the latter process resulting from a fully dynamic and spontaneously rupturing
163 seismic event while considering the effect of $\sigma_p'(\underline{x}, t)$, we refer the reader to Jin & Zoback (2018a,
164 2018b). In this study, we are concerned only with the inter-seismic evolution of induced seismicity
165 but not the co-seismic dynamic changes (i.e., wave propagation), therefore, instead of solving for
166 both $\sigma_p'(\underline{x}, t)$ and $\sigma_s'(\underline{x}, t_j^* + \delta t_j)$ for updating the fracture stress, we will instead solve only for $\sigma_p'(\underline{x},$

167 *t*) and then insert it into a stress updating algorithm to indirectly account for seismicity-induced
168 stress changes on a fracture. The details of these two steps are given in the following two sections.

2.2 Fracture-Poro-Mechanical Modeling

170 The objective here is to calculate $\sigma_p'(\underline{x}, t)$ as an input for updating the fracture stress. As mentioned
171 above, $\sigma_p'(\underline{x}, t)$ must be solved for together with the associated fluid pressure $p(\underline{x}, t)$ in a fully
172 coupled manner. Aside from the full coupling itself, another major challenge lies in that both are
173 a function of the arbitrary network of pre-existing fractures spanning over a wide range of scales.
174 While accounting for all fractures is probably computationally intractable, the subset of fractures
175 at a scale comparable to the size of the model domain of interest must be deterministically
176 resolved, as they have amply been demonstrated to have a first-order control of the modeling
177 outcome (Berkowitz, 2002; Vujevic´ et al., 2014; Hirthe & Graf, 2015; Hardebol et al., 2015). We
178 hereinafter refer to these fractures as the *large-scale deterministic fractures* (*LSDF*), which can be
179 expressed as:

$$LSDF = \bigcup_I^N F_I \tag{8}$$

181 where F_I *is the I*[th] large-scale fracture and *N* is the total number of large-scale fractures.

182 We will also refer to the step solving for the fully coupled $\sigma_p'(\underline{x}, t)$ and $p(\underline{x}, t)$ by considering the
183 *LSDF* as the *fracture-poro-mechanical modeling*. Within the framework of Biot's theory of
184 poroelasticity, Jin & Zoback (2017) formulated the problem of fluid-solid fully coupled quasi-
185 static poromechancis of an arbitrarily fractured and deformable porous solid saturated with a
186 single-phase compressible fluid. Several key governing equations together with a brief
187 description can be found in appendix A.1. This model is adopted here. To investigate the effect
188 of the *LSDF* and the effect of poroelastic coupling on seismicity, we construct the following three
189 progressive cases, each physically more representative than the previous, see Table 1.

190 **Table 1.** Three progressive cases

Case	Governing equations	Description
1	equations (A7), (A3)	Fluid diffusion in a porous medium
2	equations (A1), (A3), (A4)	Fluid diffusion in a fractured porous medium (adding the effect of the *LSDF* to case 1)
3	equations (A1)-(A5)	Coupled fluid diffusion and solid stressing in a fractured poroelastic medium (adding the effect of poroelastic coupling to case 2)

191 Case 1 states a standard fluid-diffusion problem in a fluid-saturated porous medium; case 2 is
192 similar to case 1 except for the addition of the *LSDF* contributing to the fluid-diffusion; case 3
193 describes an otherwise complete poroelastic problem in a fractured medium except for the
194 exclusion of equation (A6), which can render the modeled stress highly heterogeneous
195 characterized by concentration, compartmentalization and apparent discontinuities (Jin &

196 Zoback, 2017). To single out the effect of poroelastic coupling, equation (A6) is not considered in
197 this study such that meaningful comparisons can be made between cases 2 and 3.

198 In seeking for a numerical solution, Jin & Zoback (2017) developed a hybrid-dimensional two-
199 field mixed finite element method for efficient space discretization while preserving the
200 distribution of a given set of deterministic fractures; the solution of the fully coupled semi-
201 discrete system is advanced in time in a fully coupled manner (as opposed to a sequentially
202 coupled manner) following a fully implicit (backward Euler) finite difference scheme; within each
203 time step, the resulting nonlinear and fully discrete equation is solved using a Newton-Raphson
204 solver. This technique is adopted for case 3. For case 1, the discretization is done in space using a
205 standard Galekin finite element method and in time using a backward Euler scheme; no
206 linearization is needed. For case 2, the discretization and linearization procedures resemble those
207 in case 3 except for the use of a single-field interpolation scheme. To illustrate the differences, for
208 cases 1-3, we give their respective semi-discrete form of the governing laws shown in Table 1 after
209 space discretization. They read:

$$\tilde{\mathbf{M}}_m \dot{\hat{\zeta}}_m + \mathbf{K}_m \hat{\zeta}_m = \underline{F}_1 \tag{9}$$

$$\left(\mathbf{M}_m + \sum_I^N \mathbf{M}_{F_I}(\hat{\zeta}_{F_I}) \right) \dot{\hat{\zeta}}_m + \left(\mathbf{K}_m + \sum_I^N \mathbf{K}_{F_I}(\hat{\zeta}_{F_I}) - \sum_J^{N_I} \mathbf{K}_{mF_J}(\hat{\zeta}_{F_J}) + \sum_K^{N_{II}} \mathbf{K}_{F_K m} \right) \hat{\zeta}_m = \underline{F}_2 \tag{10}$$

$$\begin{bmatrix} \mathbf{M}_m + \sum_I^N \mathbf{M}_{F_I}(\hat{\zeta}_{f_I}) & -\mathbf{C}^T \\ \mathbf{0} & \mathbf{0} \end{bmatrix} \begin{Bmatrix} \dot{\hat{\zeta}}_m \\ \dot{\underline{d}}_m \end{Bmatrix} + \begin{bmatrix} \mathbf{K}_m + \sum_I^N \mathbf{K}_{F_I}(\hat{\zeta}_{F_I}) - \sum_J^{N_I} \mathbf{K}_{mF_J}(\hat{\zeta}_{F_J}) + \sum_K^{N_{II}} \mathbf{K}_{F_K m} & \mathbf{0} \\ \mathbf{C} & \mathbf{G}_m \end{bmatrix} \begin{Bmatrix} \hat{\zeta}_m \\ \underline{d}_m \end{Bmatrix} = \begin{Bmatrix} \underline{F}_3 \\ \underline{Y} \end{Bmatrix} \tag{11}$$

213 where $\tilde{\mathbf{M}}$ and $\mathbf{M}$ are the fluid storage capacity matrix without and with the presence of fractures,
214 $\mathbf{K}$ is the hydraulic conductivity/transferability matrix, $\mathbf{G}$ is the stiffness matrix, $\mathbf{C}$ is the coupling
215 matrix, $\underline{F}_1$, $\underline{F}_2$ and $\underline{F}_3$, which take different forms, are the external nodal mass for cases 1-3, $\underline{Y}$ is the
216 external nodal force, $\hat{\zeta}$ and $\underline{d}$ are the nodal fluid pressure and solid displacement vectors,
217 subscripts 'm' and 'F' indicate quantities associated the porous matrix and the *LSDF*, subscripts
218 'mF' and 'Fm' indicate matrix-to-fracture and fracture-to-matrix interactions, I and N are the same
219 as in equation (8), and J and K are the index of a fracture within the so-called *type-I* and *type-II*
220 subsets and N_I, N_{II} are the respective number of fractures, $N_I + N_{II} = N$. The detailed expressions of
221 the above matrices and vectors can be found in Jin & Zoback (2017). $\tilde{\mathbf{M}}$, $\underline{F}_1$, $\underline{F}_2$ can be obtained by
222 removing the fracture effect and/or the coupling effect from their respective counterparts.

223 Solving the respective fully discrete form of equations (9)-(11) allows us to calculate $\sigma_p'(\underline{x}, t)$ as an
224 input for the subsequent seismicity modelling. For cases 1 and 2, $\sigma_p'(\underline{x}, t)$ is in a standard tensor
225 notation and it reads, following a compressive stress/pressure positive notation as is used in this
226 study, the following:

227
$$\boldsymbol{\sigma}_p{'}(\underline{x},t) = -\alpha\hat{\zeta}(\underline{x},t)\mathbf{1} \tag{12}$$

228   where α is the Biot-Willis coefficient, and $\mathbf{1}$ is the Kronecker delta (see also appendix A.1).

229   and for case 3, $\boldsymbol{\sigma}_p{'}(\underline{x}, t)$ is in the so-called Voigt notation and it is calculated from $\underline{d}(\underline{x}, t)$ as:

230
$$\boldsymbol{\sigma}_p{'}(\underline{x},t) = \mathbf{D}\mathbf{B}\underline{d}(\underline{x},t) \tag{13}$$

231   where $\mathbf{B}$ is standard displacement-strain transformation matrix and $\mathbf{D}$ is the elastic stiffness
232   matrix.

2.3 Seismicity Modeling

234   The main task here is to update the stress on fractures resulting from $\boldsymbol{\sigma}_p{'}(\underline{x}, t)$ and, if seismicity
235   occurs, from $\boldsymbol{\sigma}_{sj}{'}(\underline{x})$. To do so, we consider a dual network of fractures, hereinafter referred to as
236   the DF. It consists of two complementary subsets A and B, where the subset A, denoted as $\widetilde{LSDF}$,
237   is an approximation to the $LSDF$ using a series of discrete fractures and the subset B is a stochastic
238   representation of small-scale fractures typically found in the surrounding hosting rock and is
239   hereinafter referred to as the $SSSF$. The above description can be summarized as:

240
$$DF = \widetilde{LSDF} \cup SSSF = \left(\bigcup_a^{n_A} f_a\right) \cup \left(\bigcup_b^{n_B} f_b\right) \tag{14}$$

241   where f_a is the ath fracture in the subset A, f_b is the bth fracture in the subset B, and n_a and n_b are the
242   respective total number of fractures.

243   The DF given by equation (14) is used for the seismicity modeling. For the reasons explained in
244   section 2.1, we will update the fracture stress first using only $\boldsymbol{\sigma}_p{'}(\underline{x}, t)$ and then correct for changes
245   due to $\boldsymbol{\sigma}_{sj}{'}(\underline{x})$. To do so, we make three assumptions. First, fracture slip causes negligible changes
246   in the effective normal stress on the fracture. This is an acceptable assumption for the area on the
247   fracture not immediately near its tips. From equation (5), this reads:

248
$$\boldsymbol{\sigma}_{sj}{'}(\underline{x}) : \underline{n} \otimes \underline{n} \approx 0 \tag{15}$$

249   Equation (15) implies that,

250
$$\boldsymbol{\sigma}{'}(\underline{x},t) : \underline{n} \otimes \underline{n} \approx \left(\boldsymbol{\sigma}_0{'}(\underline{x}) + \boldsymbol{\sigma}_p{'}(\underline{x},t)\right) : \underline{n} \otimes \underline{n} \tag{16}$$

251   On the other hand, the shear stress on the fracture stated by equation (6), when accounting for
252   the effect of $\boldsymbol{\sigma}_{sj}{'}(\underline{x})$, can be re-written in the following form:

253
$$\sqrt{\left\|\boldsymbol{\sigma}{'}(\underline{x},t)\cdot\underline{n}\right\|^2 - \left(\boldsymbol{\sigma}{'}(\underline{x},t):\underline{n}\otimes\underline{n}\right)^2} = \sqrt{\left\|\left(\boldsymbol{\sigma}_0{'}(\underline{x})+\boldsymbol{\sigma}_p{'}(\underline{x},t)\right)\cdot\underline{n}\right\|^2 - \left(\left(\boldsymbol{\sigma}_0{'}(\underline{x})+\boldsymbol{\sigma}_p{'}(\underline{x},t)\right):\underline{n}\otimes\underline{n}\right)^2} - \sum_j \Delta\tau_j \tag{17}$$

254 Here, $\Delta\tau_j$ is the shear stress drop on the fracture due to the jth co-seismic interval. Our second
255 assumption reads:

$$\Delta\tau_j = r\Delta\tau_{j\max} \tag{18}$$

257 Here,

$$\Delta\tau_{j\max} = (\mu_s - \mu_d)\left(\boldsymbol{\sigma}_0{}'(\underline{x}) + \boldsymbol{\sigma}_p{}'(\underline{x},t_j^*)\right):\underline{n}\otimes\underline{n} \tag{19}$$

259 In equations (18) and (19), μ_d is the dynamic frictional coefficient of the fracture as is typically
260 used in a slip-weakening law (Andrews, 1976), $\Delta\tau_{j\max}$ is the maximum likely shear stress drop and
261 r is a stochastic parameter between 0 and 1 to account for the potential non-full degree of shear
262 stress drop (see also Verdon et al., 2015). In this study, we let the probability density function of
263 r follow a uniform distribution. Equations (18) and (19) state that (1) the new shear stress on a
264 fracture due to seismicity is constrained above a lower bound defined by the residual frictional
265 strength of the fracture and (2), more importantly, the maximum likely shear stress drop is
266 dictated by the evolution of the poroelastic stress. This is different from directly prescribing the
267 shear stress drop (e.g., Izadi & Elsworth, 2014).

268 Based on the above two assumptions, we propose the following incremental fracture stress
269 updating algorithm, as is shown in List 1.

270 **List 1.** Incremental fracture stress updating algorithm for the seismicity modeling

```
for fracture fi % within the DF, equation (14)
    for time step tk
        get σp'(fi,tk) , σp'(fi,tk-1)  % section 2.2
        get σ'n(fi,tk-1) , τ(fi,tk-1) , CFF(fi,tk-1) from tk-1
        predict σ̃'n(fi,tk) , τ̃(fi,tk) , C̃FF(fi,tk) from σ'(fi,tk)=σp'(fi,tk)+σ0'(fi)  % equations (5)-(7)
        % incremental poroelastic stress compensation on the fracture (inter-seismic)
            σ'n(fi,tk)=σ'n(fi,tk-1)+(σ̃'n(fi,tk)−σ'n(fi,tk-1))
            τ(fi,tk)=τ(fi,tk-1)+(τ̃(fi,tk)−τ(fi,tk-1))
            CFF(fi,tk)=CFF(fi,tk-1)+(C̃FF(fi,tk)−CFF(fi,tk-1))
        % correction for seismicity-induced shear stress drop on the fracture, if any (co-seismic)
            if CFF(fi,tk)≥0
                Δτ(fi,tk)=r(μs−μd)σ'n(fi,tk) % equations (18), (19)
                τ(fi,tk)=μsσ'n(fi,tk)−Δτ(fi,tk)  % update the fracture shear stress
                CFF(fi,tk)=τ(fi,tk)−μsσ'n(fi,tk)=−Δτ(fi,tk) % update the fracture CFF
                nos=nos+1 % number of seismic cycle
                record and calculate seismic source parameters % appendix A.2
            end
    end
end
```

271   In List 1, the fracture f_i needs to be associated with a stress tensor $\boldsymbol{\sigma}_p{}'(f_i, t)$. Since f_i can intersect

272   multiple elements (or Gauss integration points if using high-order finite elements), as the third

273   assumption, we will use only the stress tensor from the element nearest to its center. The above

274   algorithm automatically considers multiple seismic cycles and therefore is naturally capable of

275   modeling repeating seismic events. We are now at a place to model fluid-induced seismicity in a

276   fluid-saturated and fractured poroelastic medium, see Figure 1 for a schematic illustration. A

277   complete seismicity catalog containing information on, e.g., the event origin time t_0, the location

278    $\underline{x}$, the shear stress drop $\Delta\tau$, the seismic moment M_0, the moment magnitude M_w, the fracture

279   length L, the initial Coulomb stress CFF_0 and the permeability change k^*, can be assembled.

280   Several key equations for calculating these parameters are outlined in appendix A.2. Notice in

281   equation (A8), a unit length along the third dimension is used. Additionally, the definitions of a

282   triggered event and an induced event are given in appendix A.3 and they will be used later for

283   classifying the modeled events.
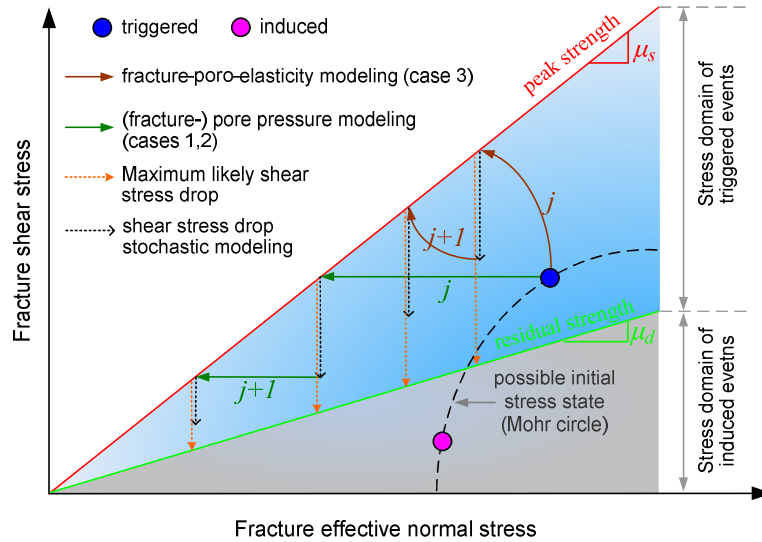
284

285   **Figure 1.** Schematic illustration (not to scale) of the hydromechanical-stochastic modeling of fluid-induced seismicity

286   in a fluid-filled and fractured poroelastic medium plotted in the fracture effective normal stress-shear stress space.

287   Based on the peak and residual frictional strengths of a fracture, as are depicted by the red and green lines, the space

288   is divided into two parts defining the initial stress domain for a triggered event and an induced event, respectively.

289   The blue and magenta dots are given as two examples, both located on a Mohr circle defined by $\boldsymbol{\sigma}_0{}'(\underline{x})$. For either type

290   of event, the seismicity modeling consists of two steps. The first step is to predict the fracture stress by compensating

291   the fracture with $\boldsymbol{\sigma}_p{}'(\underline{x}, t)$, which requires the pore pressure modeling for case 1, the fracture-pore pressure modeling

292   for case 2 and the fracture-poro-mechanical modeling for case 3, the latter two resolving the *LSDF*. The outcome of this

293   step is indicated by the green and red arrows. The second step, which does not vary among the three cases, is to

294   stochastically model $\Delta\tau$ on the fracture as indicated by the dashed arrows to approximately account for the effect of

295    $\boldsymbol{\sigma}_{sj}{}'(\underline{x})$; meanwhile, $\Delta\tau$ remains constrained on a range $\Delta\tau_{max}$ as is indicated by the yellow arrows and it is computed

296   from $\boldsymbol{\sigma}_p{}'(\underline{x}, t)$ in conjunction with $\boldsymbol{\sigma}_0{}'(\underline{x})$. Two consecutive seismic cycles *j* and *j+1* are shown, and the complete stress

297   updating scheme is given in List 1.

3. Model Set-up

3.1 Step 1 for Fracture-Poro-Mechanical Modeling

298

299

300 As a numerical example, we construct a 200 m × 200 m 2D domain representing a fracture-hosting
301 porous rock. For cases 2 and 3, we resolve a *LSDF* with 100 members with their length ranging
302 from 20 m to 50 m, and orientation, from 0 to 360°, see Figure 2a. The model domain is then
303 discretized in space, see Figure 2b, to arrive at the semi-discrete forms given by equations (10)
304 and (11). For case 1, no fracture is present; nevertheless, for meaningful comparisons, the same
305 mesh is used for arriving at equation (9). For cases 2 and 3, the nominal model parameters,
306 including the hydraulic and mechanical properties, the coupling coefficient (i.e., the Biot-Willis
307 coefficient α), the fluid and solid boundary values and the time-stepping parameter are identical
308 to those in Jin & Zoback (2017). Of our particular interest is the hydraulic diffusivity of the hosting
309 rock and the *LSDF* in cases 2 and 3, which are 9.95×10^{-4} m^2/s and 6.64 m^2/s, respectively. For case
310 1, the parameters are also the same except for the permeability of the hosting rock, which is 23
311 mD, leading to a hydraulic diffusivity D_h = 0.03 m^2/s. The rationale behind the choice of this
312 number is explained in section 4.3. For all cases, a plane strain assumption is made.

313
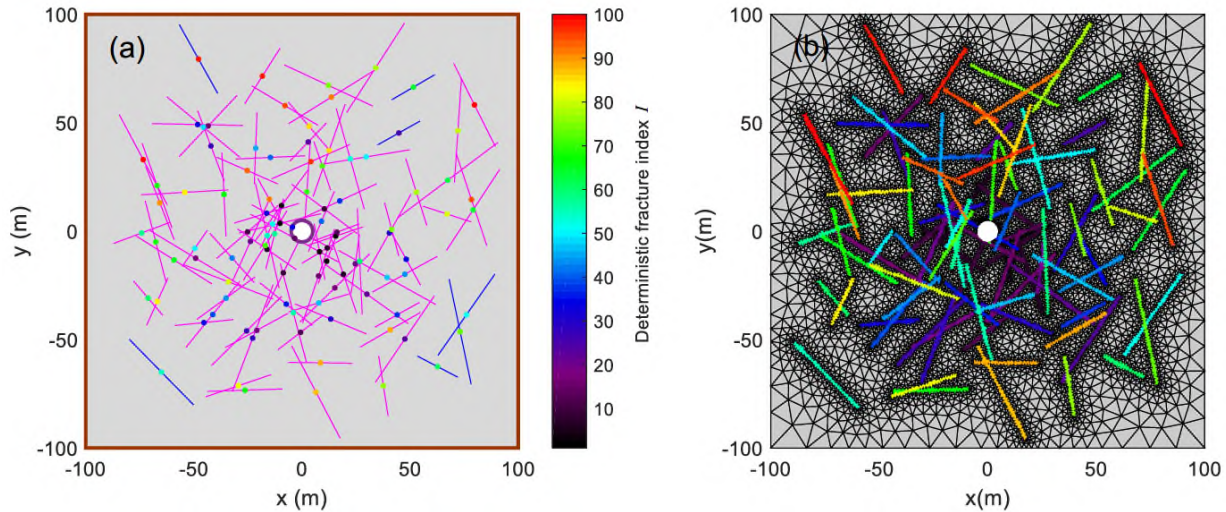
Figure 2. (a) The model domain for cases 2 and 3. It consists of a *LSDF* embedded within an otherwise porous matrix.
Each dot represents the center of the associated fracture, and the color suggests the index *I* (see equation (8)). Magenta
and blue lines represent interconnected and isolated fractures in relation to the fluid boundaries (or the external fluid
source) as are depicted by the purple circle and the dark red lines; they require different treatment of the mass exchange
with the surrounding matrix. For case 1, the *LSDF* is removed from the domain. (b) Conforming space discretization
of the fractured domain and the resulting unstructured triangular finite elements used in arriving at the semi-discrete
forms. For case 3, all elements represent the porous hosting rock; the grey elements are the standard two-field (fluid
pressure, solid displacement) mixed FE elements; the colored elements are 'hybrid' mixed elements in which at least
one edge is also used as a lower-dimensional element to discretize the fractures; the color of an element indicates the
*I*th deterministic fracture with which it is associated. If a hybrid element conforms to multiple fractures, only the largest
I is used for coloring. For case 2, the elements have similar meanings as in case 3 except they are no longer mixed (i.e.,

325 only used for interpolating the fluid pressure). For case 1, all elements are the standard single-field elements. Adapted
326 from Jin & Zoback (2017).

3.2 Step 2 for Seismicity Modeling

328 The next step is to set up the DF for the seismicity modeling, see Figure 3, and this involves two
329 sub-steps, see equation (14). Take cases 2 and 3 for example, the first sub-step is to approximate
330 the $LSDF$ shown in Figure 2a with a $\widehat{LSDF}$ as the subset A, see Figure 3a, by honoring the original
331 locations and orientations. The second sub-step is to construct a $SSSF$ in the hosting rock as the
332 subset B, see Figure 3b; in principle, this can be derived from a statistical model if data is available.
333 In this example, for simplicity and this does not change the generality of our method, we assign
334 only one fracture to each element center shown in Figure 2b as the modeling of fracture locations;
335 for subset A, the orientations are the same as the associated deterministic fracture; for subset B,
336 the orientations are randomly generated following a uniform distribution on [0, 360°]. Subsets A
337 and B constitute the complete DF for the seismicity modeling, see Figure 3c. In this process, the
338 fracture length is generated by obeying the following well-established scaling relation, which
339 states that the number of fractures within a natural fracture system scales with the fracture length
340 according to a power law (e.g., Bonnet et al., 2001; Johri & Zoback, 2014; Jin & Zoback, 2015b):

341 $$N = CL^{-D} \tag{20}$$

342 where N is the number of fractures of length L, C is a site-specific constant and D is the so-called
343 fractal dimension and a typical value is between 1 and 2. In this study, $C=1.6861$ and $D=1.0015$
344 (further details in section 4.5.2).

345 The generated L is randomly distributed to all fractures shown in Figure 3c. For case 1, the above
346 two sub-steps are repeated, however, in the first sub-step, the fracture orientations no longer
347 honor the original ones. The resulting two subsets of fractures are shown in Figures 3d and 3e
348 and the complete DF is shown in Figures 3f.
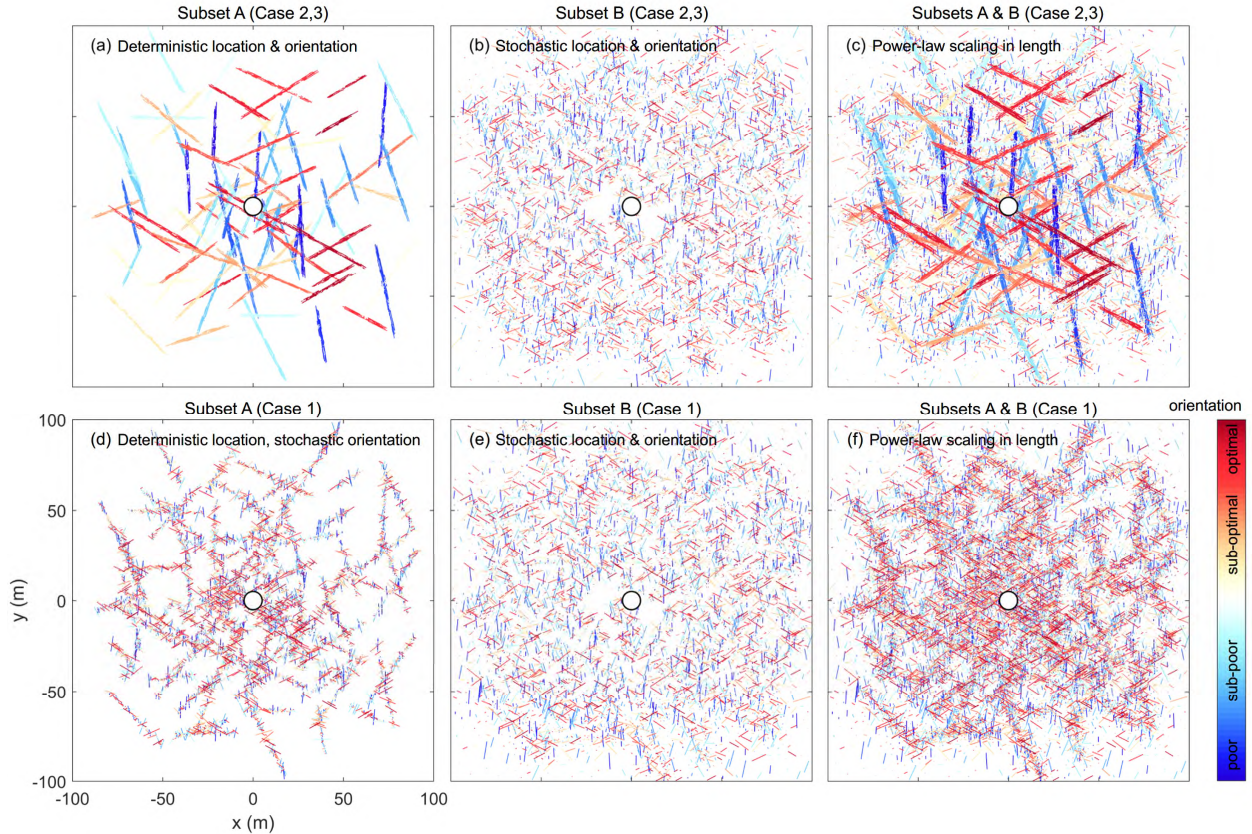
Figure 3. The dual fracture network (*DF*, equation (14)) consisting of 12800 fractures used for the seismicity modeling, shown together with its two subsets A and B. (a)-(c) Cases 2 and 3, and (d)-(f) case 1. Figures 3(a) shows the subset A with deterministic fracture locations and orientations as an approximation to the *LSDF* shown in Figure 2a; Figure 3(b) shows the subset B as a stochastic realization of fractures in the hosting rock; Figure 3(c) shows the hybrid deterministic-stochastic *DF* in which the fracture length distribution follows a realistic power-law scaling relation. Figures 3d-3f resemble Figures 3a-3c except for the stochastic fracture orientation in Figure 3d. In all figures, the warm color indicates the fracture is favorably oriented with respect to σ_0' whereas the cool color indicates otherwise.

For all cases, the same parameters are used: μ_s =0.6, μ_d =0.4 and σ_0'= [15 0; 0 5.05] MPa. Under the given σ_0', the initial effective normal stress and shear stress on all fractures are calculated, forming a Mohr circle, see Figure 4a, where the color indicates the associated initial Coulomb stress CFF_0. The same color scale is used in Figure 3 to show the susceptibility of a fracture to slip with respect to σ_0'. The peak and residual frictional strengths, calculated from μ_s and μ_d, respectively, are also shown in Figure 4a. Figure 4a also indicates that the domain is nearly critically stressed. Figure 4b shows the distribution of CFF_0, which is no longer uniform, despite a uniform distribution in the fracture orientation.

365
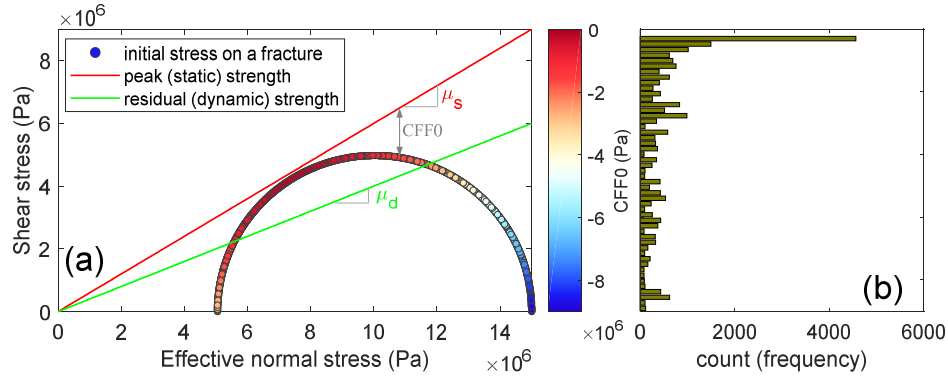
Figure 4. The initial stress used for the seismicity modeling. In Figure 4a, the initial effective normal stress and shear stress on all fractures (Figures 3c, 3f) are plotted. Because the fractures uniformly sample all likely orientations, a Mohr circle is formed. The color indicates CFF_0. The peak and the residual strengths are also shown for reference (same as those in Figure 1). The geometric meaning of CFF_0 is shown for one fracture as an example. Figure 4b is the histogram of CFF_0.

4. Results

4.1 Fluid Pressure, Poroelastic Stress and Seismicity

Figures 5 shows four snapshots of the distribution of p (Figures 5a-5d) and the associated seismicity (Figures 5e-5h) for case 1. p diffuses radially outward with a smooth and circular *overpressure front* (Shapiro et al., 1997), leading to a similar radially progressive distribution in the seismicity. However, this case has two differences from the diffusion-only statistical class of models (Shapiro et al., 2005). First, instead of using a predefined critical pore pressure value following a uniform distribution, we use predefined fractures with uniformly distributed orientations. Because the orientation needs to be transformed through equations (5)-(7), the resulting CFF_0 and the equivalent critical pore pressure, $\mu_s \times CFF_0$, follow a radically different distribution (Figure 4b), therefore, the seismicity distribution here is indeed different. Second, the use of predefined fractures further allows for the calculation of the seismic source parameters, including M_w and $\Delta\tau$ as are also shown in Figures 5e-5h.

384
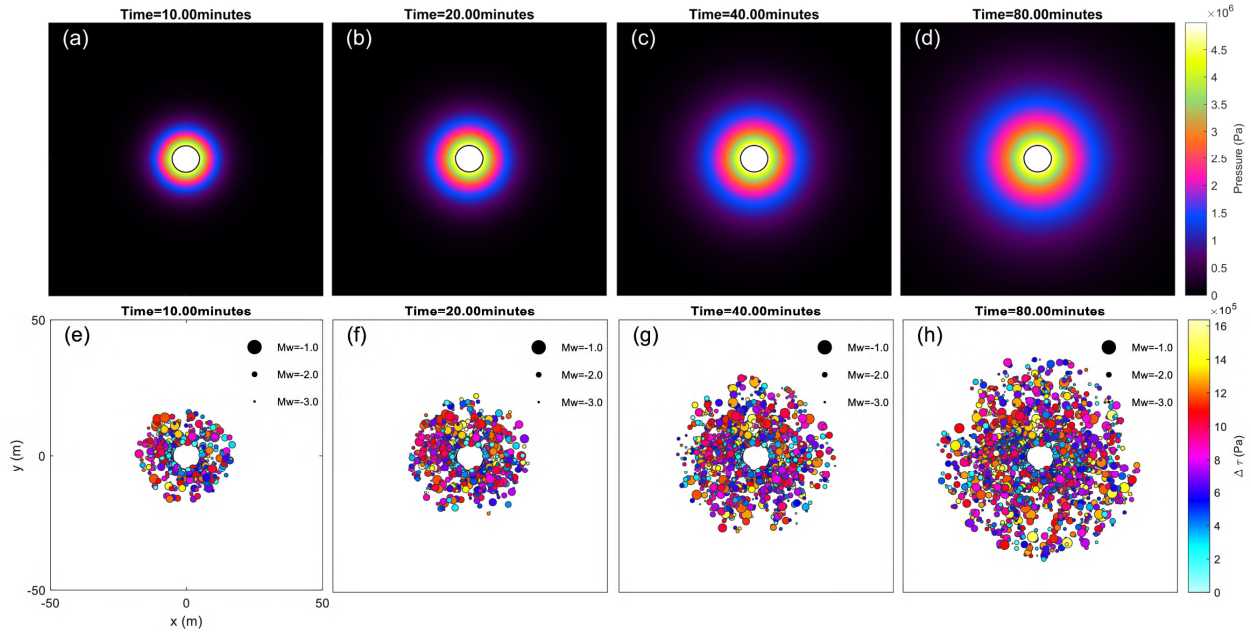
Figure 5. Snapshots of the spatial distribution of the modeled quantities at four time steps for case 1. (a)-(d) The fluid overpressure p and (e)-(f) the seismicity sized with M_w and colored with $\Delta\tau$. Only the 100 m × 100 m area around the center is shown. The time is indicated at the top of each plot.

Figure 6 shows the same snapshots of the same two quantities for case 2. Here, the effect of the *LSDF* (Figures 2a) becomes evident. First, p increases primarily along those fractures and secondarily within the hosting rock, leading to a highly non-smooth overpressure front (Figures 6a-6d). Compared to case 1, p here has a lower magnitude due to the *LSDF* diverting the fluid from the injector. Such a distribution leads to the clear clustering of the seismicity (Figures 6e-6h). Second, the distribution of the seismicity is not coincident with that of p; instead, the clustering occurs only along certain fractures. By further examining the fracture orientation (Figure 3a), we observe that the seismicity is clustered near those that are well-oriented or sub-well-oriented with respect to $\boldsymbol{\sigma}_0'$ and meanwhile subjected to sufficient p.
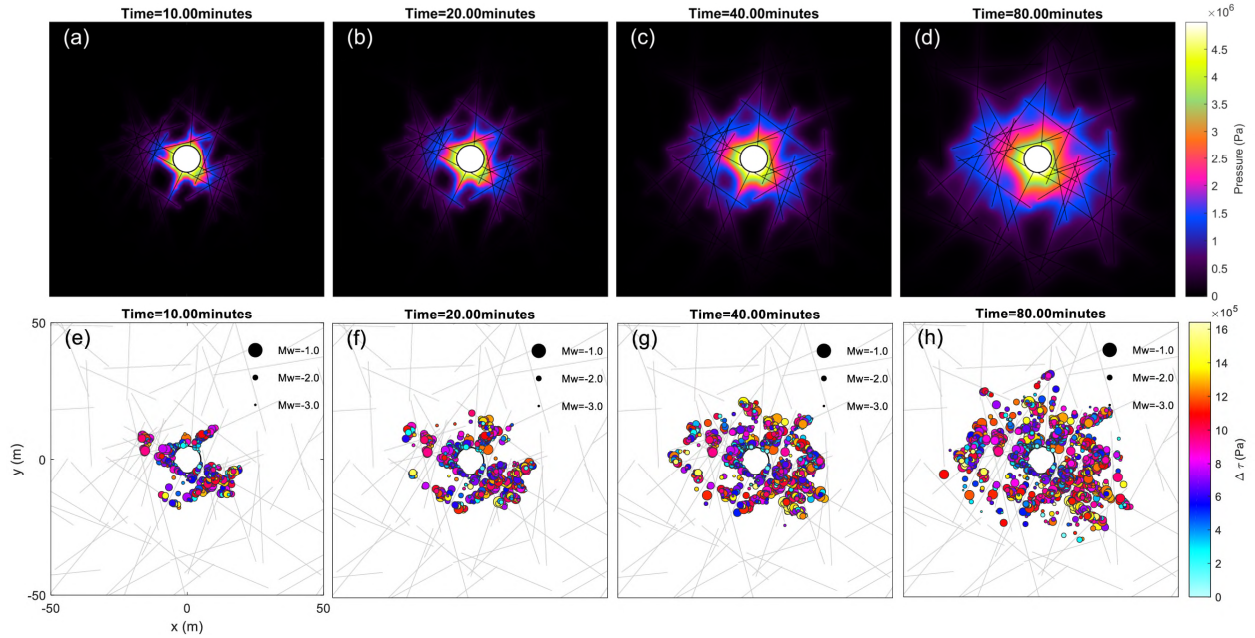
Figure 6. Same as Figure 5, but for case 2. The *LSDF* is shown in the background.

Figure 7 shows the results for case 3. The distribution of p (Figures 7a-7d) and the seismicity (Figures 7q-7t) are shown together with three other quantities, including (1) the first poroelastic stress invariant $I_1'/3$ (Figures 7e-7h), (2) the second deviatoric poroelastic stress invariant $\sqrt{J_2'}$ (Figures 7i-7l) and (3) the excess poroelastic shear stress invariant $\sqrt{J_2'}-sin(\phi)I_1'/3$ (Figures 7m-7p). All three quantities are calculated from $\boldsymbol{\sigma}_p'$ under plane strain (appendix A.4). Here, compared to case 2, the effect of poroelastic coupling is shown. First, the distribution of p is visibly different; the front of p is suppressed and the magnitude becomes lower. Second, the poroelastic normal stress $I_1'/3$ develops, dominantly being extensional near the fluid-penetrated fractures; however, the magnitude of $I_1'/3$ is lower than that of its counterpart from the decoupled approach which predicts $I_1'/3 \approx$ -0.67p (see appendix A.4) using p from case 2. Third, a pronounced shear stress field $\sqrt{J_2'}$ also develops and influences an even larger portion of the domain beyond the region subjected to $I_1'/3$ and p, whereas its counterpart in case 2 is 0. Fourth, as a result, the distribution of $\sqrt{J_2'}-sin(\phi)I_1'/3$ is different than its counterpart in case 2, which is 0.34p (appendix A.4). Specifically, within the p front (delineated in case 2, not case 3), the magnitude is lower; outside the p front, it still prevails. This observation has important implications: within the fluid-pressurized region (i.e., in the near field), poroelastic coupling tends to inhibit seismicity; outside this region (i.e., in the far field), it can either remotely promote or inhibit seismicity depending on the fracture orientation. The reason behind the former is that a fracture within the fluid-pressurized region acts as preferred flow channel, leading to a discontinuous equivalent body force (-$\alpha\nabla p$) acting away from it on the two sides, and therefore, inhibiting shear mode failure by unclamping it (Chang & Segall, 2016a; Jin & Zoback, 2016b; Jin & Zoback, 2017). This is reflected by the modeled seismicity. Like in case 2, here the seismicity is

421 clustered near fractures favorably oriented with respect to $\boldsymbol{\sigma}_0'$ and meanwhile subjected to
422 sufficient $\sqrt{J_2'}$-$sin(\phi)I_1'/3$. Notice the clustering is further enhanced by poroelastic coupling. More
423 importantly, the number of events in the near field is substantially reduced. In the far field, $\sqrt{J_2'}$-
424 $sin(\phi)I_1'/3$ turns out to be minor and only a small number of events are remotely induced. Overall,
425 the event population is reduced to only around 1/3 of that in case 2. These observations are
426 further elaborated in section 4.3.
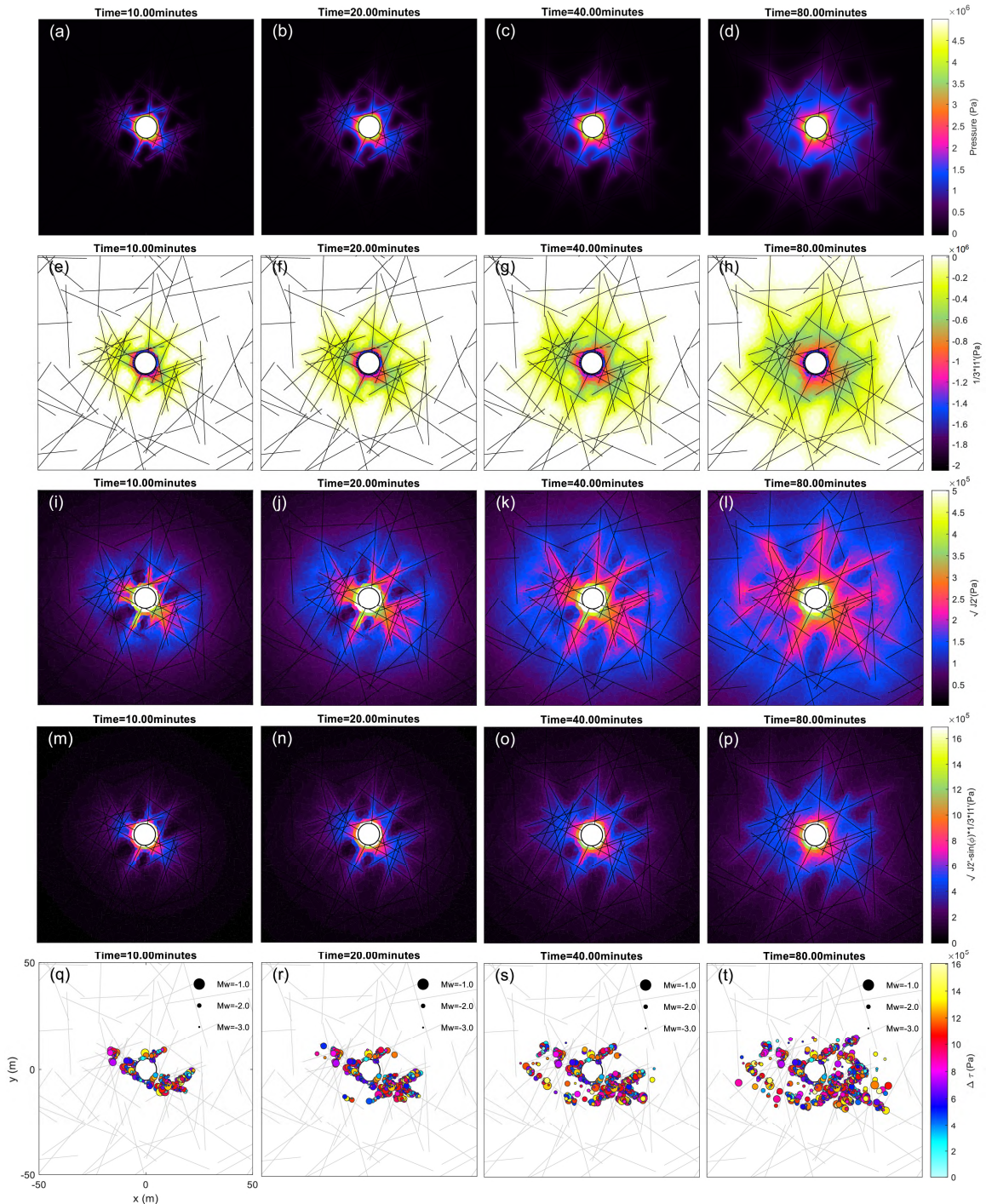
427

428 **Figure 7.** Snapshots of the spatial distribution of the modeled quantities at four time steps for case 3. (a)-(d) The fluid
429 overpressure p, (e)-(h) the first poroelastic stress invariant $I_1'/3$, (i)-(l) the second deviatoric poroelastic stress invariant
430 $\sqrt{J_2'}$, (m)-(p) the excess poroelastic shear stress invariant $\sqrt{J_2'}-sin(\phi)I_1'/3$ and (q)-(t) the seismicity sized with M_w and
431 colored with $\Delta\tau$. Only the 100 m × 100 m area around the center is shown. The time is indicated at the top of each plot.
432 The *LSDF* is shown in the background.

433 In Figures 5-7, the seismicity distribution shows increasing heterogeneity from cases 1 to 3. The
434 clustering of the events, as is frequently corroborated by field observations (e.g., Baisch & Harjes,
435 2003; Stabile et al., 2014; Deichmann et al., 2014; Block et al., 2015), can only be modeled by
436 resolving the *LSDF*. Additionally, we observe that the delineated *seismicity front* (Shapiro et al.,
437 2005) is within the p front in cases 1 and 2 and within the $\sqrt{J_2'}-sin(\phi)I_1'/3$ *front* in case 3. This is
438 because the domain is nearly critically stressed and even for the most optimally oriented
439 fractures, a sufficient amount of p or $\sqrt{J_2'}-sin(\phi)I_1'/3$ needs to be generated before triggering
440 seismicity. We note here a 'front' is only used qualitatively and it refers to where changes in a
441 quantity become visible. The modeling here highlights the importance of accounting for the
442 interactions among fractures, the initial stress and poroelastic coupling.

4.2 Event Classification

444 Figure 8 shows the spatial-temporal evolution of all modeled events sized with M_w and colored
445 with the event origin time t_0 for cases 1-3. The simulated duration of injection is 90 minutes. In
446 addition to the spatial heterogeneity, the clustering and the event population reduction as
447 explained in section 4.1, here the events also exhibit complex distribution in time for all cases. To
448 better understand these events, we categorize them into different groups and compare the results
449 among cases 1-3, as are shown through Figures 9 to 12.
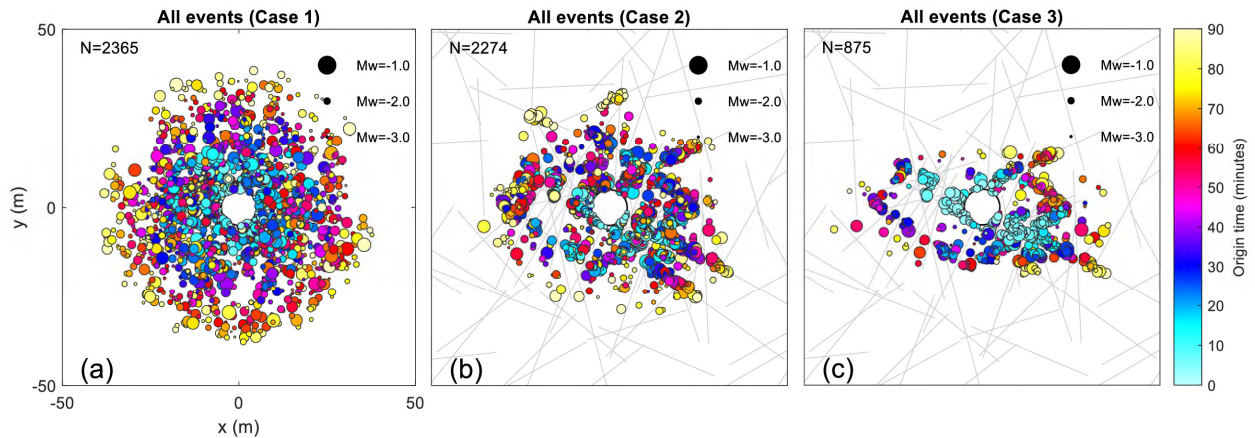
451 **Figure 8.** All events occurred within 90 minutes since the injection sized with M_w and colored with t_0. (a) Case 1, (b)
452 case 2 and (c) case 3. Only the 100 m × 100 m area around the center is shown. The number of events is indicated at the
453 top left. The *LSDF* is shown in the background for cases 2 and 3.
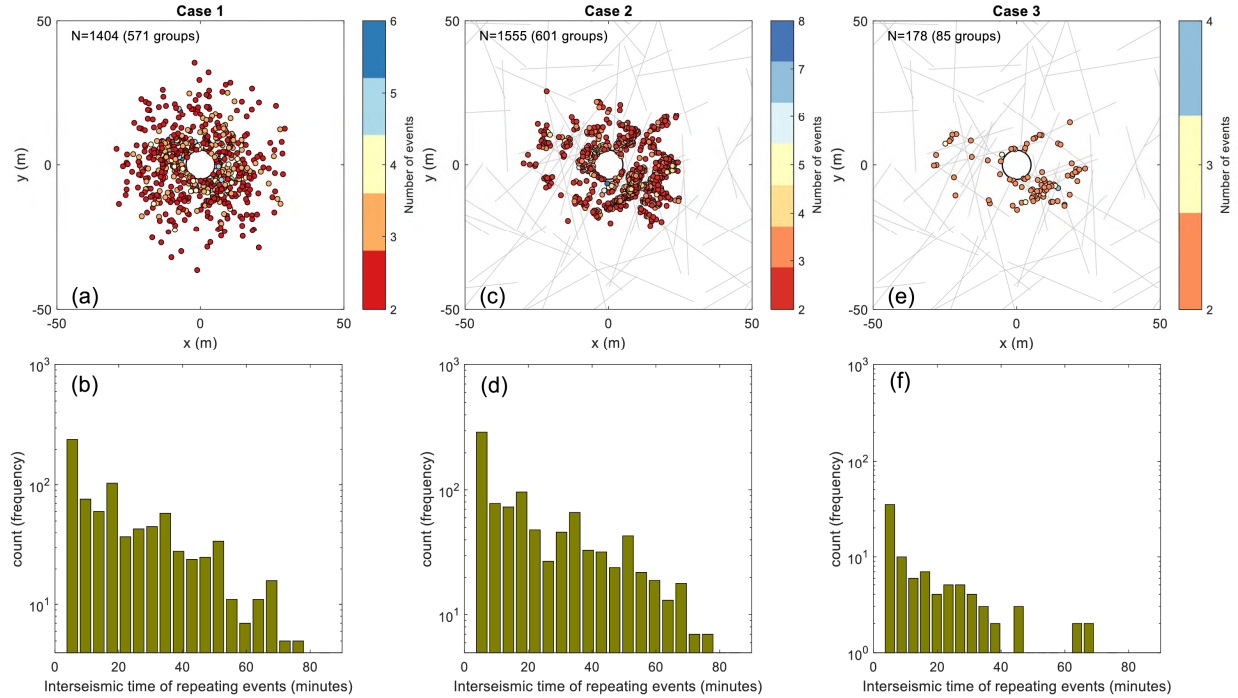
4.2.1 Repeating Events

Because we incorporated the poroelastic stress into seismic cycles, our model naturally produces
repeating events, see Figure 9. Each location indicates a doublet pair or a multiplet group (e.g.,
Poupinet & Ellsworth, 1984; Waldhauser & Ellsworth, 2002) which contains two or more events
that occur on the same source location but at different time; for visibility, a small-magnitude event
is always plotted within a big-magnitude one (see the concentric circles). The repeating events
exhibit some characteristics in space similar as those discussed in section 4.1. For example, the
overall distribution is radial in case 1 but are clustered near favorably oriented fractures subjected
to sufficient p or $\sqrt{J_2'}$-$sin(\phi)I_1'/3$ in case 2 or 3. In any case, they are concentrated in areas with a
high event density. Further, despite the difference in the spatial pattern, the number of groups
and the total number of events are similar between cases 1 and 2, suggesting the *LSDF* controls
the distribution but probably not the population of the repeating events. In case 3, however, both
drop significantly, suggesting poroelastic coupling inhibits the occurrence of repeating events as
well in the near field. Finally, within each group, an earlier event does not necessarily have a
larger magnitude; the contrary is not uncommon. This is due to the complex stress path (section
4.4) and the non-full degree of stress drop as is reflected by the r in equation (18).
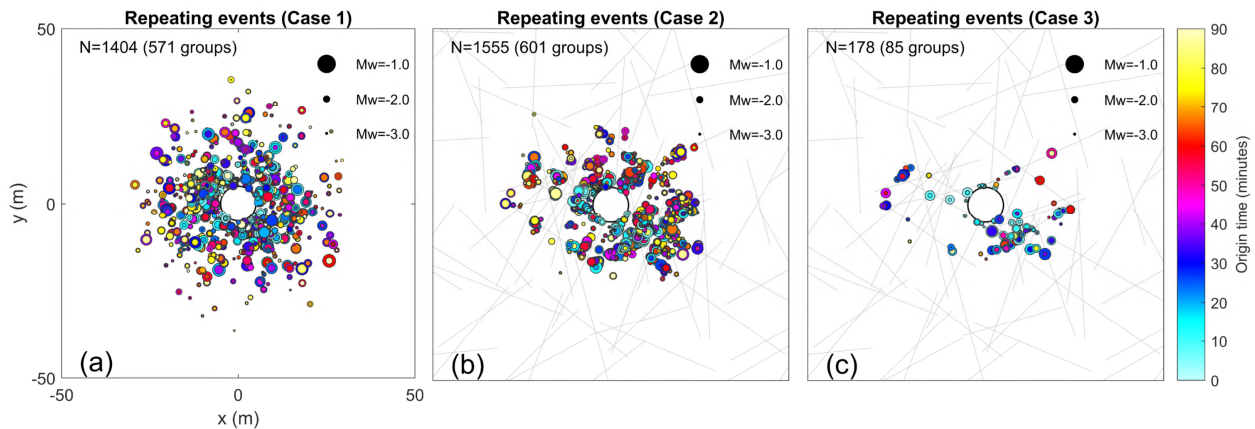
Figure 9. Repeating events sized with M_w and colored with t_0. (a) Case 1, (b) case 2 and (c) case 3. Only the 100 m × 100 m area around the center is shown. The number of groups and the total number of events are indicated at the top left. The *LSDF* in the background for cases 2 and 3.

To further understand the repeating events, we analyze the number of events within each group
and the associated inter-seismic time, see Figure 10. From Figures 10a, 10c and 10e, one observes
that in all cases, the repeating events are primarily doublet pairs; multiplet groups are present,
and the number of events within these groups suggests that p can drive a fracture through up to
8 seismic cycles within the simulated duration of injection; this number is reduced if poroelastic
coupling is considered. For the entire catalog, the inter-seismic time between any two consecutive
repeating events are compiled. The results are plotted in Figures 10b, 10d and 10f. The frequency
drops approximately linearly with respect to the inter-seismic time for all cases and appears to be
independent from fractures and poroelastic coupling.

Figure 10. Characteristics of the repeating events. (a)-(b) Case 1, (c)-(d) case 2 and (e)-(f) case 3. Figures 10a, 10c and 10e show the location of each group containing repeating events, colored with the number of events within that group (i.e., the number of seismic cycles the associated fracture has undergone). Figures 10b, 10d and 10f are histograms showing the distribution of the inter-seismic time between two consecutive repeating events.

4.2.2 Explicit and Implicit Events

We also separate the events occurring along the *LSDF* (Figures 3a) from those within the hosting rock (Figures 3b), hereinafter referred to as the *explicit* and *implicit* events, respectively. Notice this classification should only apply to cases 2 and 3. The results are plotted in Figure 11. In both cases, the explicit events well depict lineation in alignment with the favorably-oriented deterministic fractures. The along-fracture distance of an explicit event correlates positively with its origin time. This is because for the same deterministic fracture, the orientation is identical and the required p or $\sqrt{J_2'}$-$sin(\phi)I_1'/3$ is the same, therefore, the progressive increase in these two (see Figures 6 and 7) causes the seismicity to develop accordingly. For the implicit events, however, this trend immediately breaks down for the very same reason: the presence of the *LSDF* and the associated heterogeneity in p or $\sqrt{J_2'}$-$sin(\phi)I_1'/3$, when acting on stochastic fractures of various orientations, lead to random spatial-temporal evolution of the seismicity within the hosting rock. Additionally, poroelastic coupling seems to have the same effect on seismicity along deterministic fractures and within the hosting rock, as are indicated by the nearly 60% reduction in the population of both types of event.
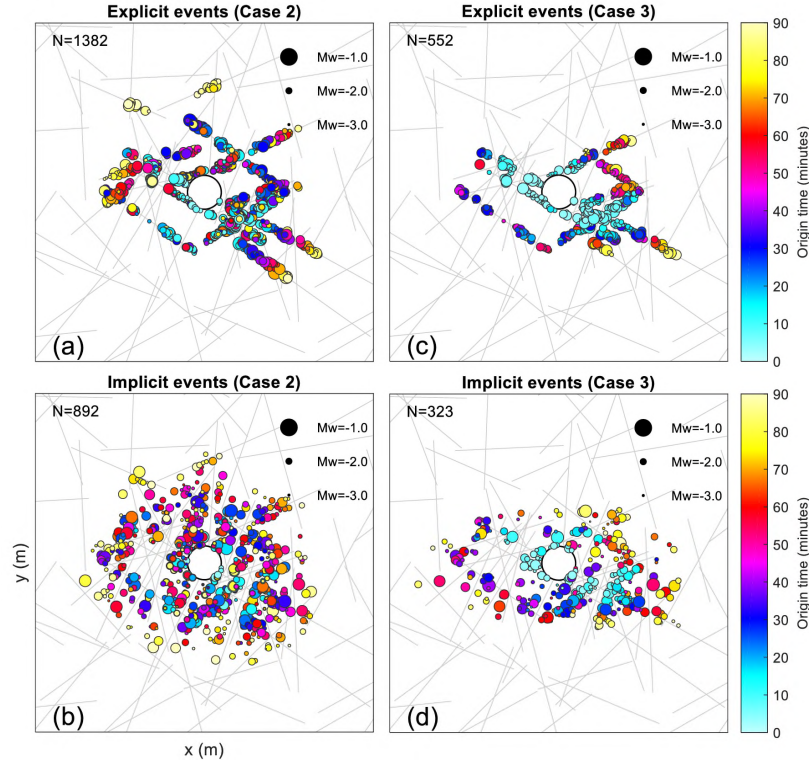
**Figure 11.** Explicit events (events along deterministic fractures) and implicit events (events within the hosting rock) sized with M_w and colored with t_0. (a)-(b) Case 2, (c)-(d) case 3. Only the 100 m × 100 m area around the center is shown. The number of events is indicated at the top left. The *LSDF* is shown in the background.

4.2.3 Triggered and Induced Events

The triggered and induced events are distinguished from each other following the definition proposed in appendix A.3 (see also Figure 1). The results are shown in Figure 12. In cases 1-3, 93.3%, 92.8% and 98.5% of the events are triggered; the remaining small number of events are induced and are distributed in close proximity to the injector, as they occur on unfavorably-oriented fractures and require a significant amount of p or $\sqrt{J_2'}\text{-}sin(\phi)I_1'/3$ to be activated. Again, for either type of event, accounting for the *LSDF* leads to the clustering and accounting for poroelastic coupling significantly reduces the number of events.
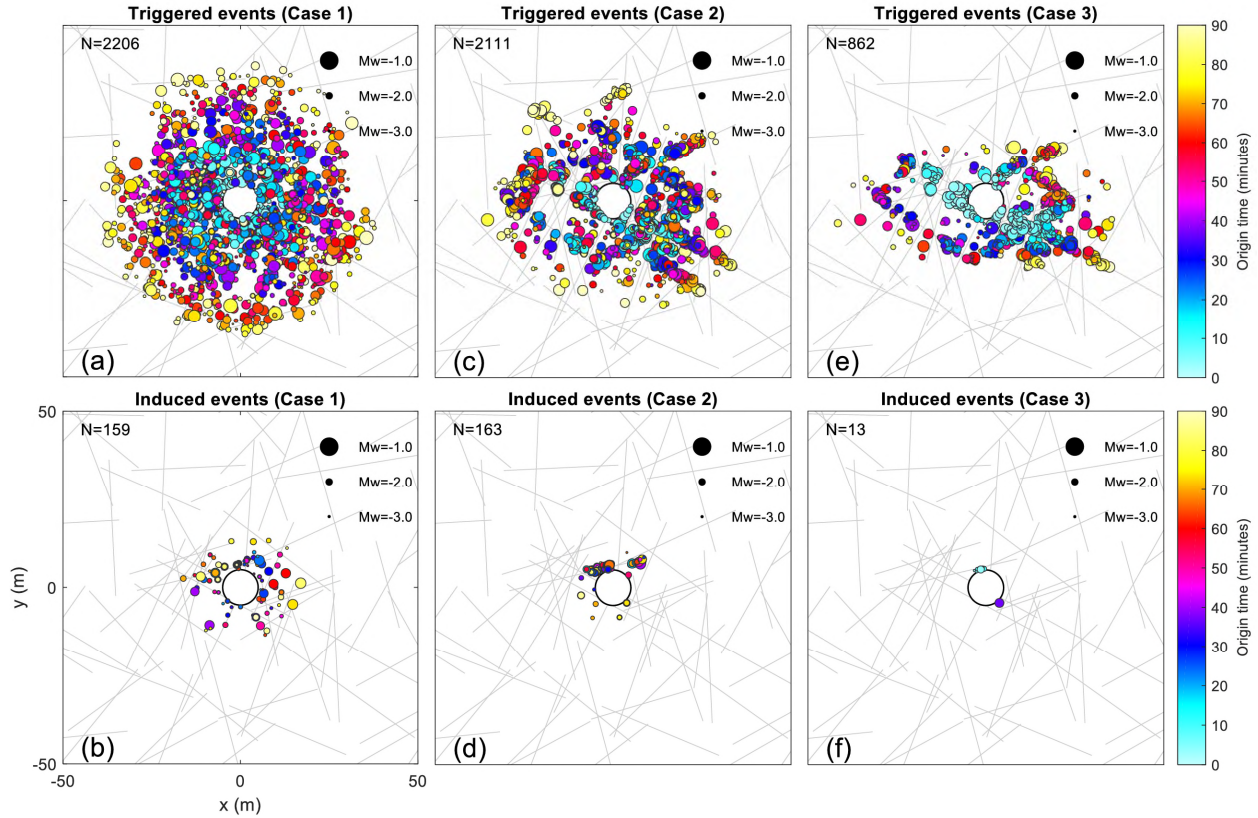
Figure 12. Triggered and induced events sized with M_w and colored with t_0. (a)-(b) Case 1, (c)-(d) case 2 and (e)-(f) case 3. Only the 100 m × 100 m area around the center is shown. The number of events is indicated at the top left. The *LSDF* is shown in the background.

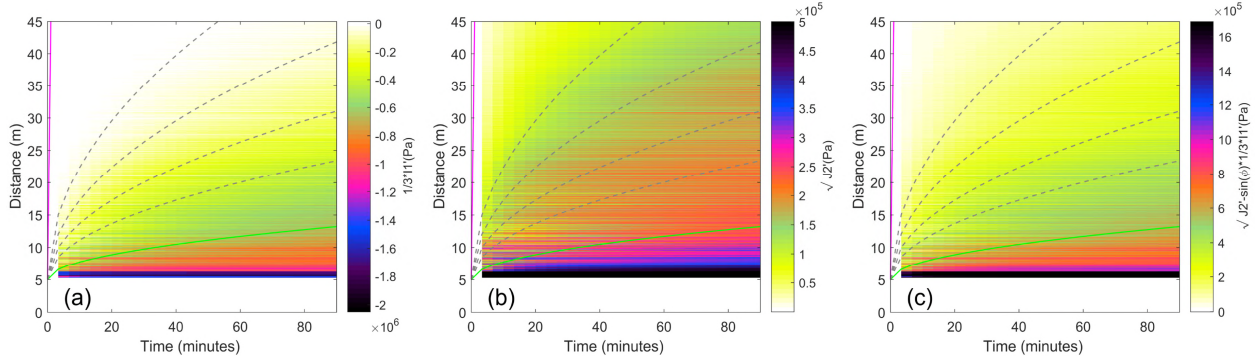## 4.3 *R-T* Characteristics

4.3.1 Fluid Pressure and Poroelastic Stress

The spatial-temporal characteristics of the modeled quantities are further illustrated using the so-called *R-T* plots shown in Figures 13-16, where R is the distance from the origin and T is the time since the beginning of the injection. p is shown in Figure 13 for cases 1-3. Overlaying are several iso-diffusivity profiles (gray dashed lines) calculated as $R=\sqrt{4\pi D_h T}+5$m where D_h is the hydraulic diffusivity; $R=\sqrt{4\pi D_h T}$ is a characteristic profile derived from a linear diffusion process resulting from a Heaviside point source injection in an isotropic, homogeneous and porous only medium, and is referred to as the so-called *seismicity triggering front* (Shapiro et al., 1997; Shapiro et al., 2002). Notice the use of such profiles should apply only to case 1 (Figure 13a). Nonetheless, for reference, they are also plotted for cases 2 and 3 (Figures 13b, 13c), where additionally, the green and magenta lines corresponding to D_h of the hosting rock and the *LSDF*, respectively, are also plotted. It is mentioned in section 3.1 that in case 1 D_h = 0.03 m²/s. We choose this value such that the modeled p front in the *R-T* space is approximately the same as that in case 2. In a sense, this value reflects the overall *effective* D_h of the fractured porous media in case 2. Case 1 shows a smooth variation of p in the *R-T* space. In case 2, however, due to the effect of fractures, strong

535 heterogeneity is introduced, in addition to an overall reduction in the magnitude of p. The effect
536 of poroelastic coupling is reflected by comparing case 2 and 3. The p front is slightly suppressed
537 and the magnitude of p is further reduced.
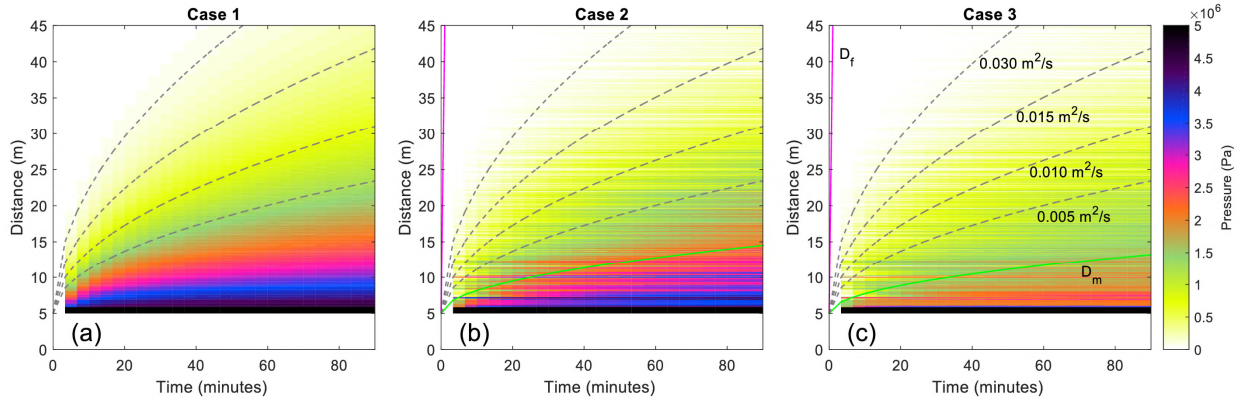
538

539 **Figure 13.** Space-time plot of the fluid overpressure p. (a) Case 1, (b) case 2 and (c) case 3. The distance is only plotted
540 from 0 to 45 m. The color scale is reserved from that in Figures 5-8. Several characteristic diffusion profiles are shown
541 (see text) as references, including the green and magenta lines calculated using the diffussivity of the hosting rock and
542 the fractures, respectively. The differnces between cases 1 and 2 show the effect of the *LSDF* and the differences between
543 cases 2 and 3 show the effect of poroelastic coupling.

544 To further illustrate the effect of poroelasic coupling, for case 3, we investigate the *R-T*
545 characteristics of the poroelastic stress invariants, see Figure 14. We observe the following. First,
546 although the spatial distributions of $I_1'/3$ and p differ (Figures 7a-7h), the delineated front of $I_1'/3$
547 (Figure 14a) coincides with that of p (Figure 13c) in the *R-T* space. This is explained by equation
548 (A1) which states that $I_1'/3$, which scales linearly with the volumetric strain $\nabla \cdot \underline{u}$, diffuses together
549 with p. Poroelastic coupling does, however, reduces the magnitude of $I_1'/3$ compared to its
550 counterpart $-0.67p$ (section 4.1 and appendix A.4) where p is given by Figure 13b. The effect of
551 poroelastic coupling is further manifested by Figure 14b, which shows the development of $\sqrt{J_2'}$
552 one-order below p in magnitude. This cannot be predicted by case 2. Also, it is evidently shown
553 that the delineated front of $\sqrt{J_2'}$ well exceeds those of p and $I_1'/3$ (Figures 13c, 14a). Figure 14c
554 results from the combination of Figures 14a and 14b. The effect of poroelastic coupling is reflected
555 by its difference in magnitude from its counterpart $0.34p$ (section 4.1 and appendix A.4) where p
556 again is given by Figure 13b. Finally, poroelastic coupling also seems to smear out the
557 heterogeneity in the stress upon comparing Figures 14a-14c against Figure 13b. Notice equation
558 (A6) is not included in our modeling.

559

Figure 14. Space-time plot of the poroelastic stress invariants for case 3. (a) $I_1'/3$, (b) $\sqrt{J_2'}$ and (c) $\sqrt{J_2'}$-$sin(\phi)I_1'/3$. The distance is only plotted from 0 to 45 m and the characteristic diffusion profiles are the same as those in Figure 13. The color scale is reserved from that in Figures 5-8. The counterparts of the three quantities in case 2 without the coupling effect can be obtained by multiplying the p in Figure 13b with -0.67, 0 and 0.34 (appendix A.4).

4.3.2 Seismicity

Figures 15 shows the *R-T* distribution of the seismicity for cases 1-3 and the color indicates CFF_0. In Figure 15a, a parabolic seismicity front is clearly delineated for case 1, showing also an evident 'lag' behind the p front (Figure 13a). This lag reflects the effect of the initials stress with respect to the static shear failure line (i.e., the peak strength, see Figure 4). Here D_h corresponding to the p front and the seismicity front are 0.03 m²/s and 0.015 m²/s, respectively. In this case, if the seismicity front was to be used to back calculate D_h (e.g., Shapiro et al., 2002), D_h would be over-estimated by 100%. This motivates some nonlinear diffusion-based interpretations which incorporate pressure-dependent D_h (e.g., Hummel & Shapiro, 2012; Hummel & Shapiro, 2013). Here, our model is mechanics-based and it does not require the somewhat unclear definition of 'a relatively large p' which underlines the diffusion-only class of statistical models (Shapiro et al., 1997). The effect of the *LSDF* can be seen in Figure 15b. Notice the increased curvature of the parabolic seismicity front, which is above the predicted characteristic profile (second grey dashed line from the top) earlier and near the injector but below this profile later and away from the injector. Hummel & Shapiro (2013) used a power-law type of pressure-dependent D_h to correct for this change. However, our model not only produces this change but also introduces additional heterogeneity. Figure 15c shows further variations by accounting for poroelastic coupling. Compared to Figure 15b, here the number of events is greatly reduced, the heterogeneity becomes much more pronounced, and some 'outliers', which are the remotely triggered events, are present but not dominant. Additionally, nearly all events are sourced from favorably-oriented fractures. The result of case 3 also shows a good agreement with a dataset provided in Hummel & Shapiro (2013). Finally, the same *R-T* plots are made using only the repeating events for cases 1-3, as are shown in Figures 15d-15f, which illustrate the 'breaking-down' of the parabolic seismicity front for repeating events. Such events are assumed to be non-existent in the diffusion-only class of statistical models.
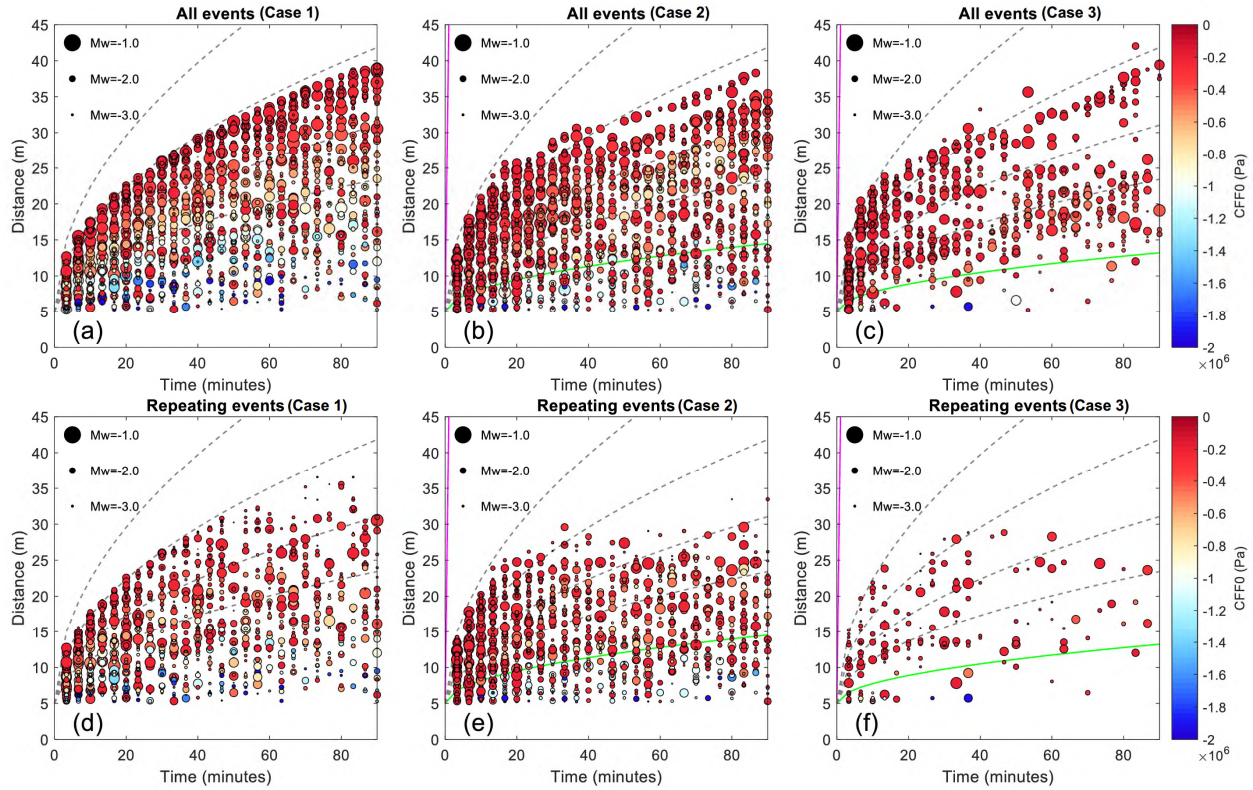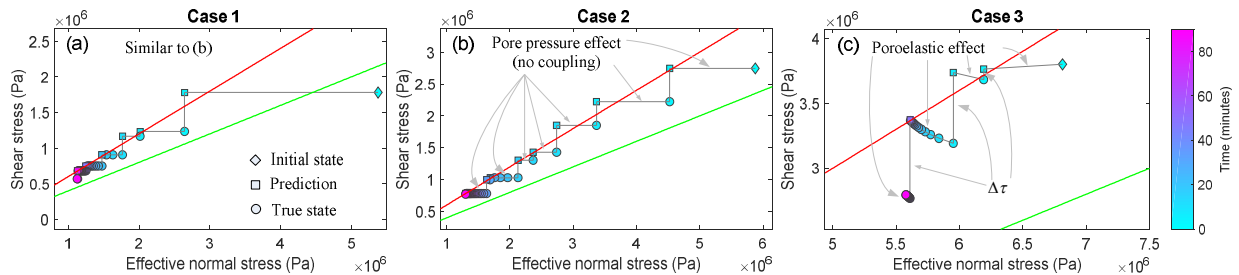
Figure 15. Space-time plot of all seismic events and repeating seismic events, sized with M_w and the colored with CFF_0, (a), (d) Case 1, (b),(e) case 2 and (c),(f) case 3. The distance is only plotted from 0 to 45 m and the reference characteristic diffusion profiles are the same as those in Figure 13. The differnces between cases 1 and 2 show the effect of the *LSDF* and the differences between cases 2 and 3 show the effect of poroelastic coupling.

4.4 Stress History

As an example, for each case, we chose one representative fracture that has generated the most repeating events and plot the associated complete stress path colored with time, see Figure 17. In all cases, p or $\sqrt{J_2'}$-$sin(\phi)I_1'/3$ are sufficient enough to drive a fracture through multiple seismic cycles within 90 minutes. However, the decoupled approach tends to over-predict the number of seismic cycles (see also Figure 10). Notice the increasingly unfavorable orientation of the fracture from cases 3 to 1. Additionally, within each seismic cycle, poroelastic coupling leads to a bended stress path in case 3 as opposed to a linear leftward one in case 1 or 2.

603 **Figure 16.** Representative complete stress paths. (a) Case 1, (b) case 2 and (c) case 3. The color indicates the time. The
604 number of seismic cycles is 6 in cases 1 and 2 and 3 in case 3. The pore pressure effect and the poroelastic effect are
605 indicated.

606 Figure 17 gives the snapshots of changes in the stress of all fractures (Figures 3c, 3f) in the σ_n'-τ
607 space for cases 1-3. We hereinafter abbreviate each σ_n'-τ pair as a NS, which is indicative of a
608 fracture. The reference state (Figure 4a) is divided into three parts, namely parts I, II and III. Upon
609 injection, the stress state on some fractures deviates from the reference state, and the relative
610 changes are shown by the grey arrows. Cases 1 (Figures 16a-16d) assumes simply the pore
611 pressure effect. As a result, p always causes a reduction in σ_n' by the amount of αp but does not
612 change τ, leading to a strict leftward translation of a NS before it reaches the peak strength and
613 CFF remains negative. When CFF reaches 0, seismicity occurs and $\Delta\tau$ is enforced. Throughout this
614 process, a NS must remain constrained below the peak strength at all time, and if seismicity
615 occurs, above the residual strength. This means a NS originated from part II remains in between
616 the green line and the red line, and a NS from part I can cross the green line if p is sufficient but
617 always stays below the red line; correspondingly, the triangular domains denoted as B and A
618 (dashed lines) define the respective possible new stress state of a fracture driven to failure from
619 parts II and I. Therefore, the pore pressure effect also predicts a positive correlation between the
620 favorability of the orientation and $\Delta\tau_{max}$. Here, any arrow with a downward component signifies
621 the seismicity only. As can be seen, the majority of the events are sourced from part II. For part
622 III, a similar triangular domain C can be defined. All the above observations hold for case 2
623 (Figures 16e-16h). However, compared to case 1, here the deviation of a NS is more discernable
624 from others due to the localization of p around the $LSDF$. The magnitude of p in general becomes
625 lower as is reflected by the less amount of leftward translation. The results of case 3 (Figures 16i-
626 16l) show the intriguing effect of poroelastic coupling. The deviation from the Mohr circle is much
627 less significant in general and the seismicity is inhibited overall. Notice the deviation of a NS is
628 now towards all directions, suggesting any combination of an increase or decrease in σ_n' and an
629 increase or decrease in τ is possible. For example, a NS from part I can undergo a left and upward
630 path towards the peak strength, rendering a larger possible $\Delta\tau_{max}$. As a result, domains A, B and
631 C can no longer be defined here. An arrow with a downward component indicates either the
632 seismicity or the poroelastic shear stress. Nonetheless, for a majority of the fractures and prior to
633 the seismicity, the leftward component still dominates over the others, suggesting the reduction
634 in σ_n' is the primary source driving up CFF.
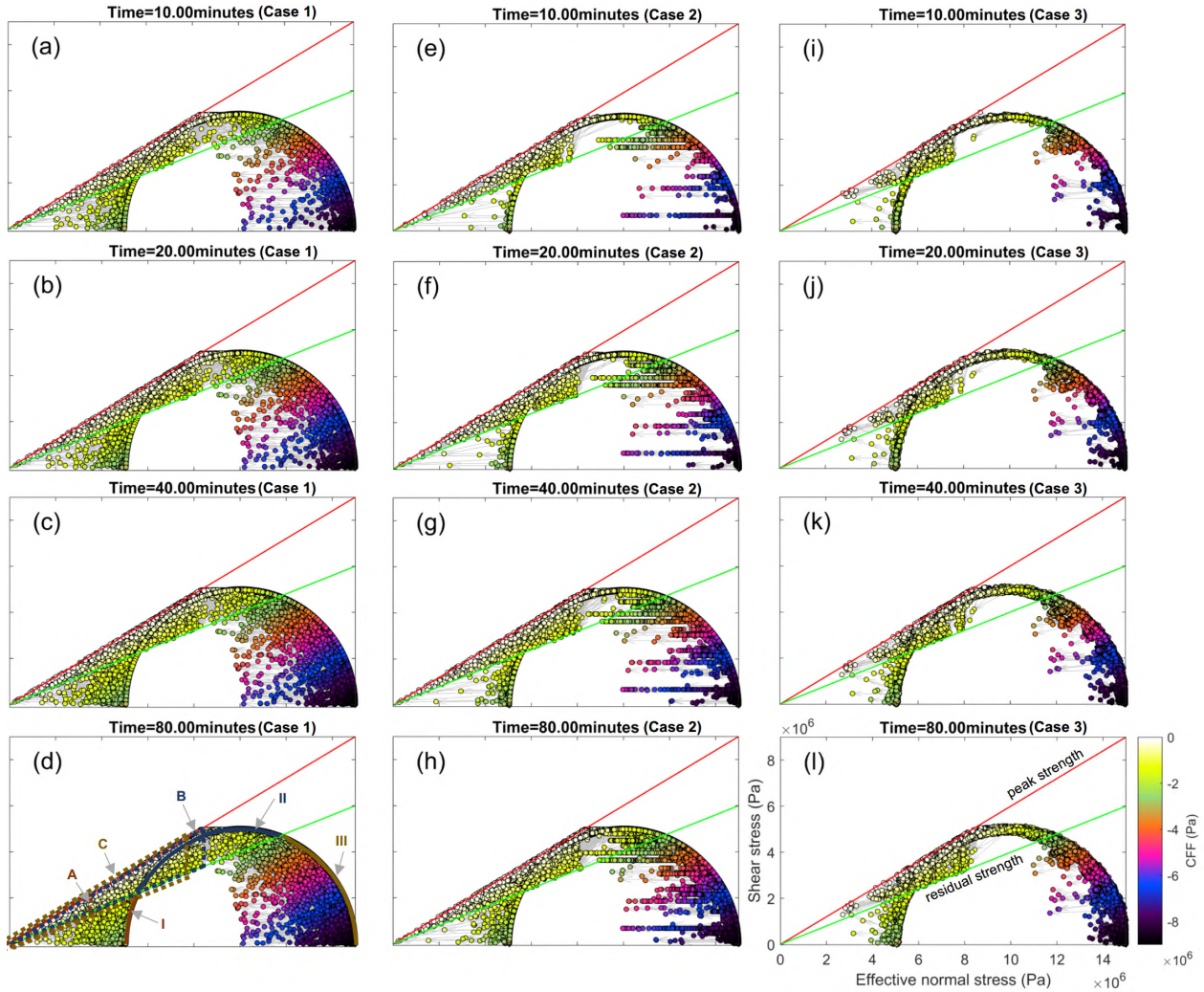
Figure 17. Snapshots of the effective normal stress and shear stress on all fractures showing the deviation from the initial reference state (the Mohr circle in Figure 4a) at four selected time steps. (a)-(d) Case 1, (e)-(h) case 2 and (i)-(l) case 3. The peak and residual strengths are shown for reference. The color indicates *CFF* and the time is indicated at the top of each plot. For each fracture, two dots corresponding the initial and new stress states are plotted, connected with an arrow indicating the relative change. The initial Mohr circle is partitioned into three parts labeled as I, II and III. The meaning of the triangular areas bounded with dashed lines are explained in the text. The differnces between cases 1 and 2 show the effect of the *LSDF* and the differences between cases 2 and 3 show the effect of poroelastic coupling.

4.5 Source Parameters

4.5.1 Stress Drop, Fracture Length and Moment Magnitude

Figures 18a, 18c and 18e summarize the modeled seismic source characteristics in the parameter space for cases 1-3. For each event, M_w is plotted against the associated fracture length L and colored with $\Delta\tau$. The modeled events, with M_w between -3 and -1, occur on fractures of L ranging from 0.1m and 10m, and $\Delta\tau$ ranges from below 0.1 MPa to above 1 MPa, consistent with many real micro-earthquake data sets (e.g., Goertz-Allmann et al., 2011; Mukuhira, 2013). Such source

651 characteristics overall seem not affected by the *LSDF* nor poroelastic coupling. For a realistic
652 range of Δτ, the parameter *r* in equation (18) turns out to be important, see appendix A.6. Figures
653 18b, 18d and 18f further show the overall similar distribution of Δτ for cases 1-3. In each case, [0.1,
654 1] MPa is the dominant range. In case 3, however, events with high Δτ (e.g., above 1 MPa) does
655 occupy a higher percentage, consistent with that poroelastic coupling can lead to a larger possible
656 Δτ$_{max}$ as demonstrated in section 4.4.
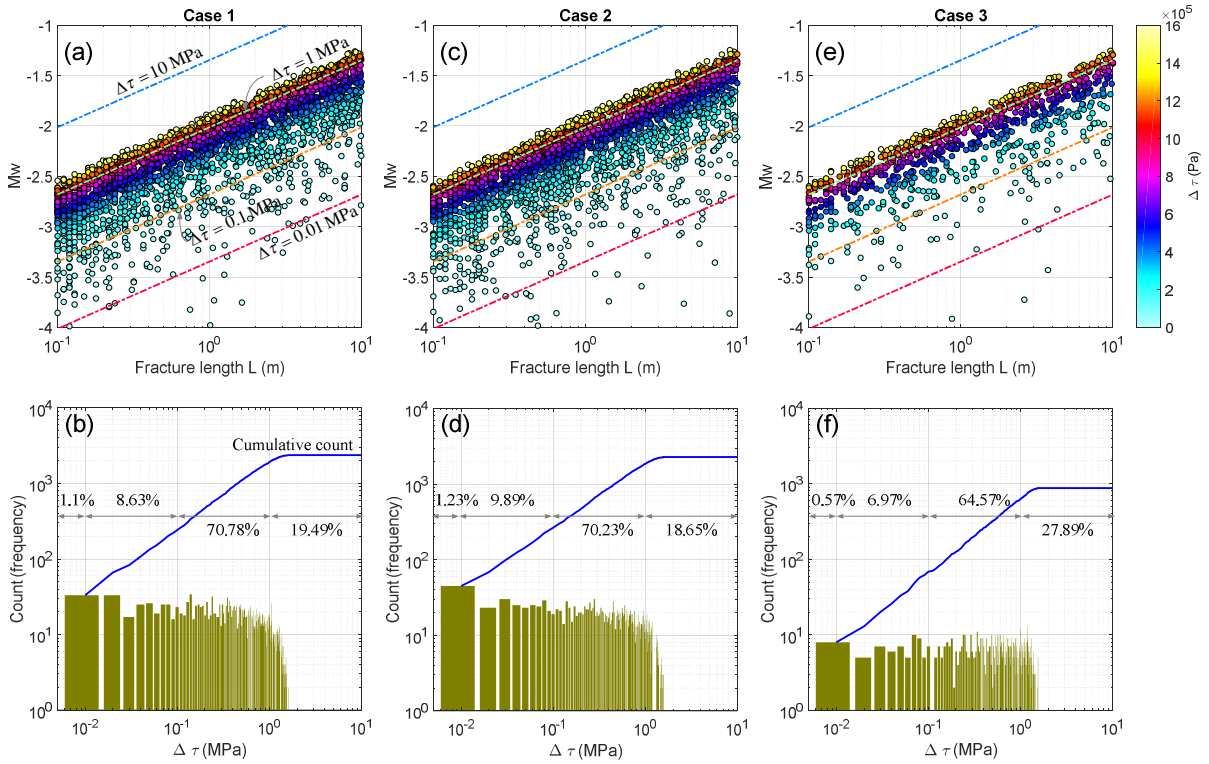
658 **Figure 18.** The top row shows relationships among M_w, L and Δτ of all modeled events. Overlaying are four contours
659 corresponding to Δτ=0.01 MPa, 0.1 MPa, 1 MPa and 10 MPa. The bottom row shows the histograms of Δτ together with
660 the cumulative frequency using 1000 equal-sized bins on the range [0.01, 10] MPa. Additionally, the number of events
661 with Δτ≤0.01 MPa, 0.01MPa<Δτ≤0.1 MPa, 0.1MPa<Δτ≤1 MPa and Δτ>1 MPa are counted and the percentages are
662 shown. (a), (b) Case 1, (c), (d) case 2 and (e), (f) case 3.

4.5.2 Magnitude-Frequency Relation

664 We have introduced a power law that describes the commonly observed scaling relation between
665 the fracture length and the frequency (section 3.2). On the other hand, earthquakes in nature are
666 characterized with a universal statistical relation between the magnitude and the cumulative
667 frequency, namely the Gutenburg-Richter law (Gutenberg, 1956), which reads:

$$\lg N(m > M_w) = a - bM_w \tag{21}$$

669 where $N(m>M_w)$ is the total number of events with a moment magnitude m above M_w, and a and
670 b are constants.

671 In nature, D is frequently observed to be between 1 and 2 (e.g., Okubo & Aki, 1987), whereas a
672 common value of b is around 1 (e.g., Shi & Bolt, 1982). Studies suggest that D and b are inherently
673 related. For example, Hirata (1989) suggests that D≈2b. What is somewhat curious is that for
674 induced seismic events, b is often above 1 (e.g., Vermylen & Zoback, 2011) and sometimes around
675 2 (e.g., Bachmann et al., 2012), although a near-1 value has also been reported (Schoenball et al.,
676 2015).

677 In Figure 19, for each case, the distribution of the length of all fractures (Figures 3c, 3f) is plotted
678 (green), together with the power law fitting line (magenta); the distribution of the length of the
679 activated subset of fractures is also plotted (red), which clearly no longer obeys the power law
680 decay, owing to that only favorably oriented fractures are induced to slip. Nonetheless, the
681 magnitude-frequency relation still holds for the induced events, as is illustrated in Figure 20. For
682 each case, the distribution of M_w, which primarily varies between -3.5 and -1.0, is shown as the
683 histogram (yellow green); the total number of events (i.e., cumulative frequency) is shown by the
684 blue-green dots, which is then used to fit the Gutenburg-Richter law, yielding a b-value around
685 2. Notice the similarities among all three cases in both figures 19 and 20, suggesting that the b-
686 value is likely to be independent from the *LSDF* and poroelastic coupling. We also hypothesize
687 that the breaking-down in the power law distribution of the length of the activated subset of
688 fractures might be responsible for the deviation in the b-value for induced seismicity.
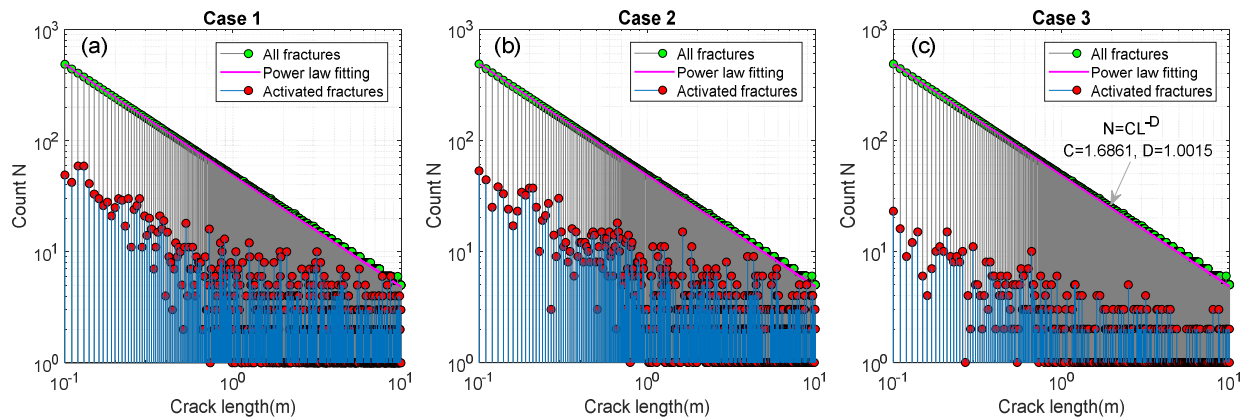
689

690 **Figure 19.** Histogram of the fracture length using 1000 equal-sized bins, plotted on a log-log scale as discrete sequences.
691 The green sequence indicates the distribution of length of all fractures, which follows a power law decay as is fitted
692 with the magenta line. The fitting parameters are also shown, specifically, the fractal dimension D is 1. The red sequence
693 shows the length distribution of activated fractures only (fractures undergone at least one seismic cycle). Because it is
694 primarily the favorably oriented fractures that are activated, the distribution no longer follows a power law decay. (a)
695 Case 1, (b) case 2 and (c) case 3.
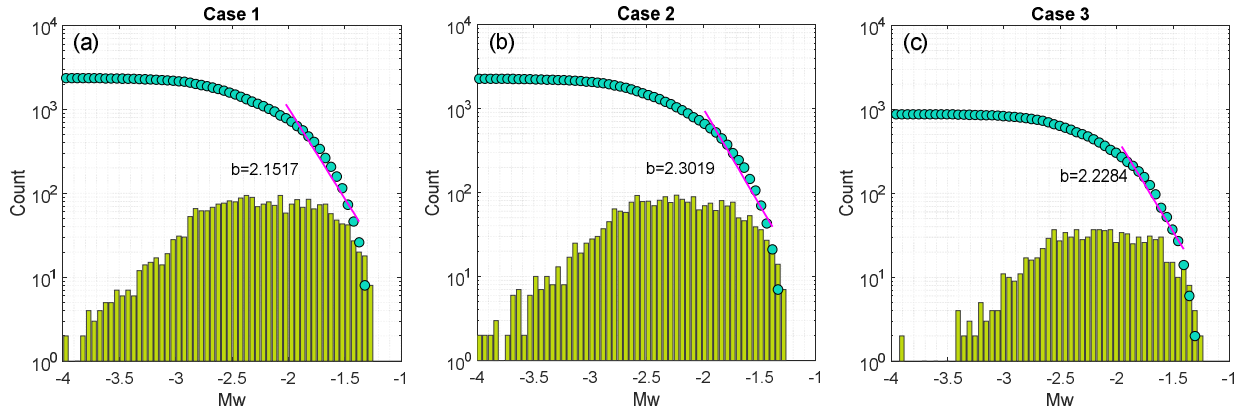
Figure 20. Histogram of the modeled M_w (yellow green). The bin size is 0.05, and the y-axis is on a log-scale. The associated distribution of N follows the classic Gutenberg-Richter law (blue green); data points with a M_w above -2 are used for fitting (the magenta line), yielding a b-value around 2, which is commonly observed for induced seismicity. (a) Case 1, (b) case 2 and (c) case 3.

Further, we investigate whether the b-value of induced seismicity exhibits spatial or temporal dependences. To do so, for each case, we divide the events into 10 groups in both space and time based on the associated distance R and the origin time t_0. For each group, we carry out the same b-value analysis as has been described above and the results are displayed in Figures 21 and 22. In each case, the magnitude-frequency distribution appears alike among all groups in both space and time. The b-value is predominantly between 2 and 2.5 and no substantial spatial- or temporal-dependence is observed. Such independences are not altered by the *LSDF* or poroelastic coupling. An exception is shown in Figures 21c and 21f, where the b-value is around 3 near the injection and drops to between 2 and 2.5 away from the injection (see also Bachmann et al., 2012), possibly due to some variations among the selected cutoff M_w for data fitting.
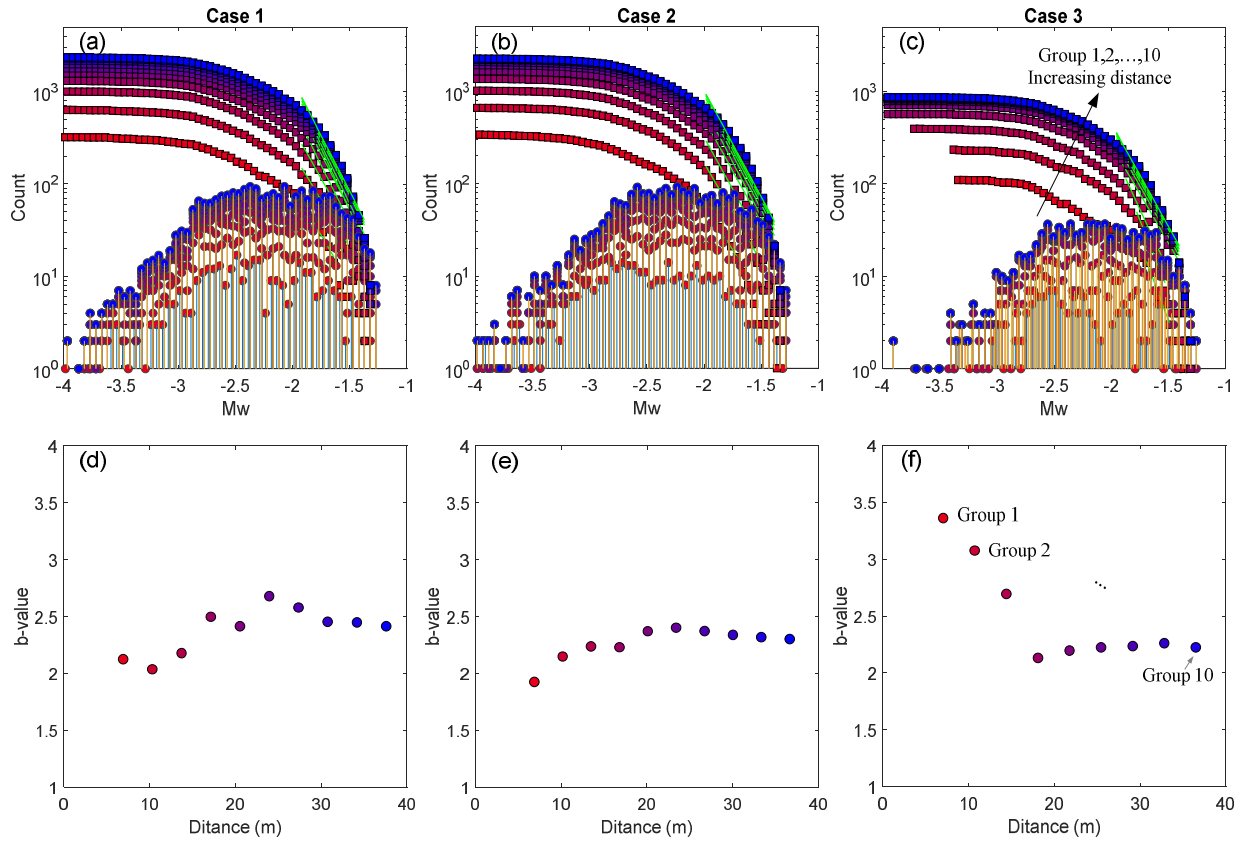
Figure 21. *b*-value analysis in space. The modeled distance interval [R_{min}, R_{max}] is divided into 10 equal-sized bins and the events are grouped accordingly. The group number is indicated by the color. A *b*-value is fitted for each group (top row, slope of the green line) and is plotted against the corresponding distance (bottom row). The cutoff M_w for fitting is around 2 but some variations exist among all groups. (a), (d) Case 1, (b), (e) case 2 and (c), (f) case 3.
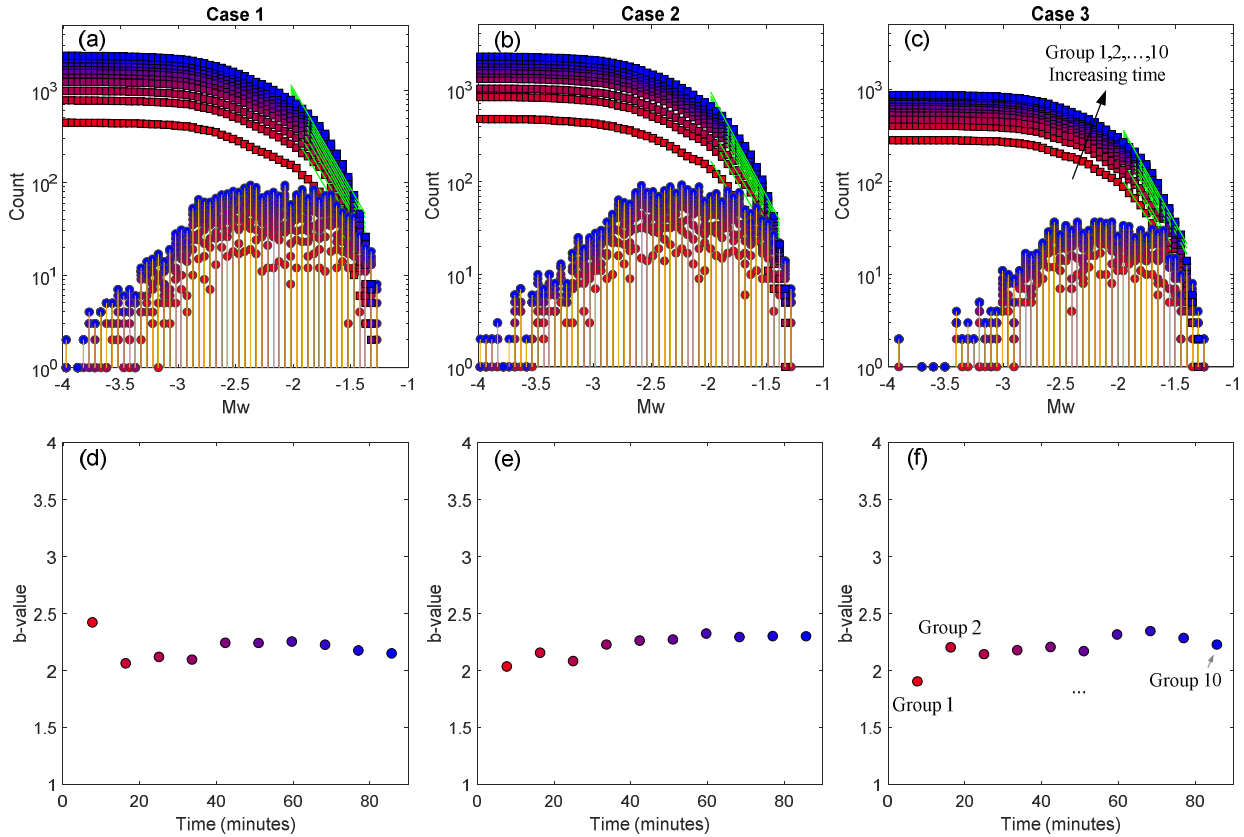
Figure 22. Same as Figure 21 but for the 10 equal-sized origin time intervals on the modeled $[t_{0\min}, t_{0\max}]$.

4.6 Activated Fractures and Permeability Enhancement

Figure 23 gives four snapshots illustrating the growth of the activated network of fractures for cases 1-3. The network consists of fractures both interconnected to and isolated from the fluid boundary. In the context of unconventional and geothermal reservoir stimulation, the interconnected fractures are indicative of the so-called stimulated reservoir volume and the stimulation efficiency. As can be seen, resolving the *LSDF* predicts localized permeability-enhanced flow channels and less area is stimulated as a result. This effect manifests itself if poroelastic coupling is further considered. For each activated fracture, the nondimensionalized permeability changes along directions perpendicular and parallel to it, denoted as $k\perp/k$ and $k_{//}/k$, respectively, are calculated from the associated M_w using a simple power law scaling relation (appendix A.2). This relation predicts a linear scaling between $k\perp/k$ and $k_{//}/k$, and therefore both can be normalized into the same quantity k^*, which indicates the color in Figure 23. As an example, we focus on ($k\perp/k$) only. For a fracture that has undergone j seismic cycles ($j>1$) at a time step of interest, $\Sigma_j(k\perp/k)$ is calculated as the result at this time step. The modeled maximum ($k\perp/k$) for a single-event fracture and a multi-event fracture are 30.6 and 81.2 for case 1, 31.1 and 76.7 for case 2 and 30.9 and 49.1 for case 3, suggesting that repeating seismic cycles can further enhance

734 the permeability by a few more folds compared to just the first seismic cycle but poroelastic
735 coupling seems to counteract this effect.
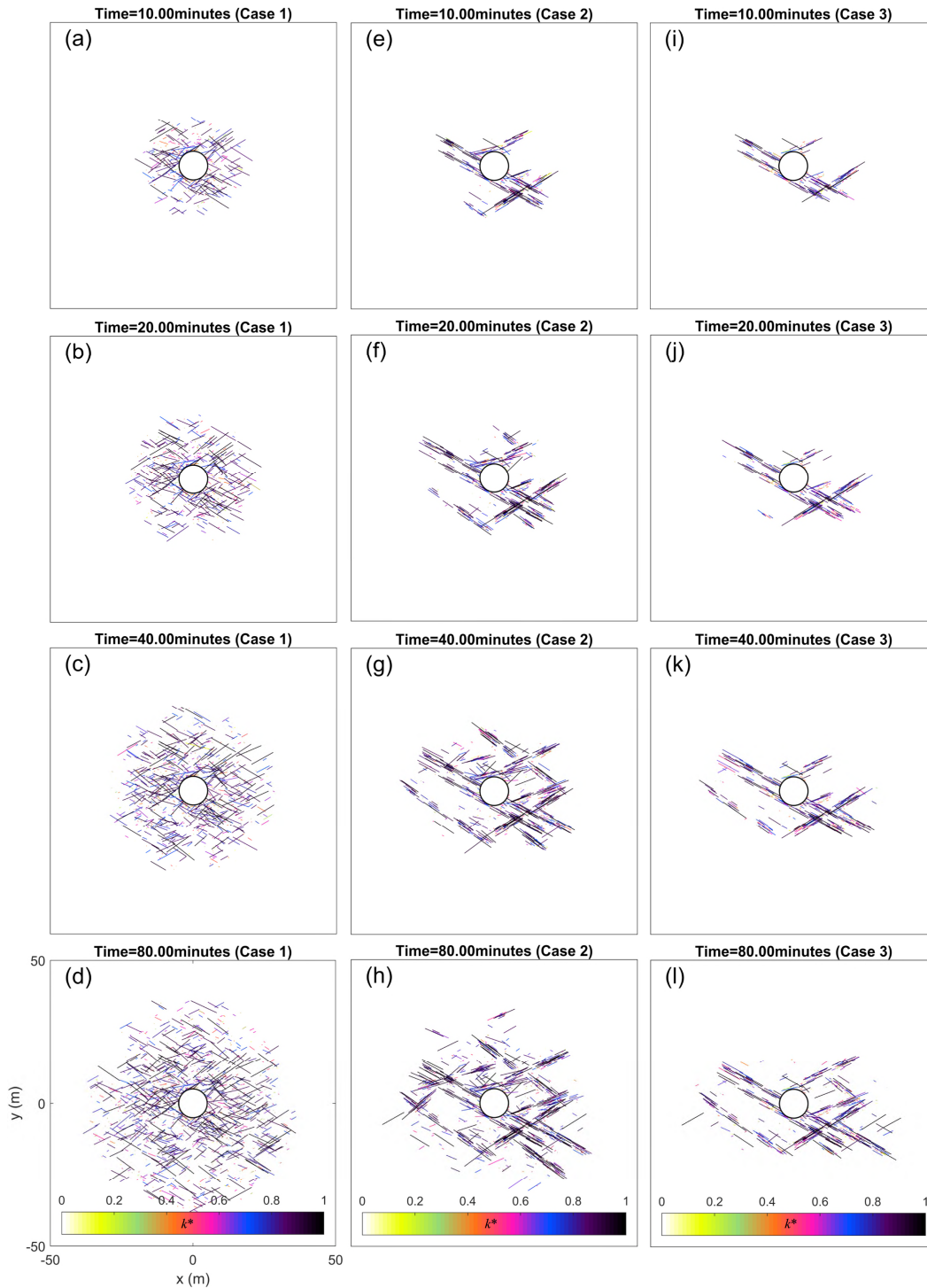
736

737 **Figure 23.** Snapshots of the activated fractures at four selected time steps showing the progressive development of the
738 stimulated network. The time is indicated at the top of each plot and the color shows the quantity $k*$ (appendix A.2),
739 which is indicative of the permeability changes along the fracture-normal and -tangential directions. (a)-(d) Case 1, (e)-

740 (h) case 2 and (i)-(l) case 3. The differnces between cases 1 and 2 show the effect of the *LSDF* and the differences between
741 cases 2 and 3 show the effect of poroelastic coupling.

5.Summary and Conclusions

743 We have developed a hydromechanical-stochastic approach to modeling fluid perturbation-
744 induced seismicity in a fluid-saturated and fractured poroelastic medium. Following predefined
745 distributions characteristic of a natural fracture system, we generate a dual network of fractures
746 consisting of large-scale deterministic fractures (*LSDF*) and small-scale stochastic fractures (*SSSF*)
747 within the hosting rock. The modeling consists of two sequential steps, including first the quasi-
748 static fracture-poro-mechanical modeling and second the seismicity modeling. In the first step,
749 only the *LSDF* is considered and it is resolved in a computational model of fluid-solid fully
750 coupled single-phase poromechanics of arbitrarily fractured media. This provides a *LSDF*-
751 controlled poroelastic stress tensor as a pivotal input for the second step, in which the complete
752 dual network of fractures is then considered. The seismicity-induced shear stress loss on a slipped
753 fracture is stochastically modeled as a static quantity without explicitly resolving the co-seismic
754 dynamic rupture process; it remains constrained within a range computed from the time-
755 dependent poroelastic stress in conjunction with the initial stress and the peak and residual
756 frictional strengths. A prediction-correction type of fracture stress updating scheme is developed
757 accordingly, which naturally produces multiple seismic cycles. Three progressive cases were
758 designed to show the effects of fractures and poroelastic coupling on the resulting seismicity and
759 its characteristics. Compared to the prevalent fracture-free, coupling-free and diffusion-only class
760 of statistical models, our method produces induced seismicity with spatial-temporal
761 characteristics agreeing much better with real data. It also goes beyond the scope of most current
762 models and provides a synthetic catalog of induced events, allowing for the analysis of seismic
763 source characteristics and connections between observations and model physics.

764 Main findings from this study are:

765 (1) The spatial-temporal evolution of the pore fluid overpressure p, the change in the solid
766 effective stress tensor $\boldsymbol{\sigma}_p'$ and the associated stress invariants, I_1', $\sqrt{J_2'}$ and $\sqrt{J_2'}$-$sin(\phi)I_1'/3$, all
767 differ in a porous medium, a fractured porous medium and a fractured poroelastic medium. In
768 space, the presence of the *LSDF*, if hydraulically conductive, leads to marked localization of these
769 quantities around it and the associated fronts become highly non-smooth. Poroelastic coupling
770 tends to reduce the magnitude of p and I_1' near fluid-penetrated fractures but predicts an
771 otherwise non-existing $\sqrt{J_2'}$ within the entire domain. As a result, $\sqrt{J_2'}$-$sin(\phi)I_1'/3$ is reduced in
772 the near field but increased in the far field. In the *R-T* space, p and I_1' share the same front which
773 is below the front shared by $\sqrt{J_2'}$ and $\sqrt{J_2'}$-$sin(\phi)I_1'/3$.

774 (2) In space, the *LSDF* leads to not only heterogeneity but also pronounced clustering in the
775 seismicity. Poroelastic coupling not only enhances the clustering, but also substantially inhibits

776 the seismicity and greatly reduces the number of events in the near field. In the far field, although
777 it can remotely trigger some events, its effect does not dominate even in the presences of critically
778 stressed fractures. Overall the event population is significantly reduced. The clustering occurs
779 only near fractures favorably oriented with respect the initial stress tensor σ_0' and meanwhile
780 subjected to sufficient amount of $\sqrt{J_2'}$-$sin(\phi)I_1'/3$. Correspondingly, the activated subset of
781 fractures forms permeability-enhanced flow channels localized along the $LSDF$, and this is further
782 manifested by poroelastic coupling. In the R-T space, the characteristics of the seismicity are in
783 good agreement with observations from real data. In addition to heterogeneity, the curvature of
784 the delineated parabolic seismicity front is increased by the $LSDF$. The state of σ_0' with respect to
785 the fracture peak strength can render the seismicity front lagged behind the p front. A positive
786 correlation is observed between the distance and the origin time for events occurring along the
787 $LSDF$ but not those occurring in the hosting rock.

788 (3) σ_p' (either coupled or decoupled with p) and seismicity are the two sources driving changes in
789 the stress on a fracture, and together they can drive the fracture through multiple seismic cycles
790 on a timescale relevant to the problem. This provides a viable mechanism of fluid-induced
791 repeating seismic events characterized with a step-wise stress path. The distribution of the inter-
792 seismic time between two consecutive repeating events seems independent from both the $LSDF$
793 and poroelastic coupling. The latter, however, tends to reduce the number of repeating event
794 groups and the number of seismic cycles within a group, in addition to adding nonlinearity to
795 the associated step-wise stress path. Repeating events are also able to increase the permeability
796 change on the fracture by a few folds.

797 (4) Although collectively referred to as induced seismicity, the modeled events are predominantly
798 triggered as opposed to induced. Because the induced events occur on unfavorably-oriented
799 fractures that require large p or $\sqrt{J_2'}$-$sin(\phi)I_1'/3$, they are concentrated near the source of the fluid
800 perturbation.

801 (5) Some source characteristics of the induced seismicity seem independent from the $LSDF$ and
802 poroelastic coupling. Irrespective of the case, the moment magnitude M_w and by extension, the
803 permeability change k^*, show similar distributions; the b-value varies between 2 and 2.5 and
804 exhibits no substantial space- or temporal-dependence; for the given set of parameters, the stress
805 drop $\Delta\tau$ predominantly falls in between 0.1 MPa and 1 MPa, although a higher $\Delta\tau$ is more likely
806 due to the poroelastic medication to the stress path. $\Delta\tau$ generally does not reach the maximum
807 likely stress drop.

808 (6) In our complete dual fracture system, the length and frequency obey a realistic power law
809 scaling relation; however, this relation no longer holds for the activated subset of fractures, owing
810 to that only favorably-oriented fractures are induced to slip. This might explain the commonly

811 observed deviation in the *b*-value from around 1 for natural seismicity to around 2 for induced
812 seismicity.

Acknowledgement

Appendix

A.1 Single-Phase Poromechanics of Arbitrarily Fractured Media

818 Jin & Zoback (2017) formulated the problem of single-phase poromechanics of fluid-saturated
819 and arbitrarily fractured porous media. Without presenting the full details, here, we outline
820 several key governing equations. First, the fully coupled mass conservation law and quasi-static
821 force balance law are:

822
$$\left(\Lambda_0(\underline{x})\phi_{m0}(\underline{x})\left(C_m + C_\rho\right) + \left(1 - \Lambda_0(\underline{x})\right)\phi_{f0}(\underline{x})\left(C_f + C_\rho\right) \right)\dot{p}(\underline{x},t)$$
$$-\alpha\nabla\cdot\dot{\underline{u}}(\underline{x},t) + \nabla\cdot\underline{v}(\underline{x},t) = s(\underline{x},t), \quad \underline{x}\in\Omega_m\cup\Omega_f \tag{A1}$$

823
$$\nabla\cdot\boldsymbol{\sigma}_p{}'(\underline{x},t) + \alpha\nabla p(\underline{x},t) = \underline{0}, \quad \underline{x}\in\Omega_m\cup\Omega_f \tag{A2}$$

824 Next, the two fluid flow equations are given by the Darcy's law and a nonlinear cubic law,
825 designated to the matrix and fractures, respectively. They read:

826
$$\underline{v}(\underline{x},t) = -\eta^{-1}\mathbf{k}_m(\underline{x})\cdot\nabla p(\underline{x},t), \quad \underline{x}\in\Omega_m \tag{A3}$$

827
$$\underline{v}(\underline{x},t) = -\eta^{-1}\frac{1}{12}\left(b_0(1 + C_f p_f(\underline{x},t))\right)^2 \nabla_\tau p(\underline{x},t), \quad \underline{x}\in\Omega_f \tag{A4}$$

828 Furthermore, the two solid constitutive laws, including a generalized Hooke's law for the hosting
829 rock and a transverse simple shear deformation law for fractures, read:

830
$$\boldsymbol{\sigma}_p{}'(\underline{x},t) = \mathbb{C}_m : \nabla^s \underline{u}_m(\underline{x},t), \quad \underline{x}\in\Omega_m \tag{A5}$$

831
$$\boldsymbol{\sigma}_p{}'(\underline{x},t) = G_{f\tau}\nabla_n u_{f\tau}(\underline{\xi},t), \quad \underline{\xi}\in\Omega_f \tag{A6}$$

832 In equations (A1) - (A6), subscripts '*m*' and '*f*' indicate quantities associated with the hosting rock
833 (porous matrix) and deterministic fractures, subscript '0' denotes the initial value of a quantity,
834 subscripts '*n*' and '*τ*' indicate the fracture normal and tangential directions, $\underline{x}$ and $\underline{\xi}$ indicate the
835 global and fracture local coordinate systems, *t* is the time, Ω is the model domain, ϕ is the intrinsic
836 porosity, $\Lambda(\underline{x})$ is a fracture-dependent parameter enabling the definition of a so-called partial
837 porosity, *C* is the compressibility, *p* is the fluid overpressure, $\underline{v}$ is the fluid velocity vector, *s* is the

838   external fluid source normalized by the initial fluid density, η is the fluid viscosity, **k** is the
839   permeability tensor, b is the fracture hydraulic aperture, $\boldsymbol{\sigma}_p{}'$ is the solid effective stress (i.e., the
840   poroelastic stress) tensor, $\underline{u}$ is the solid displacement vector, a is the Biot-Willis coefficient, **1** is the
841   Kronecker delta, $\mathbb{C}$ is the elastic stiffness tensor under plane strain and G is the fracture shear
842   modulus. ∇, ∇^s, ∇_n and ∇_τ are operators for computing the gradient, the symmetric gradient, the
843   fracture-normal gradient and the fracture-tangential gradient, and $\nabla\cdot$ is the divergence operator.

844   The presence of fractures is reflected in equation (A1) by the modification to the hydraulic storage
845   capacity, and by equations (A4) and (A6) as the augmentation to the hydraulic conductivity and
846   the elastic stiffness of the system. Fracture-induced nonlinearity is introduced by equation (A4)
847   via the pressure-dependent hydraulic aperture. Additionally, by formulating the problem over a
848   single domain, the mass exchange between fractures and the matrix is resolved by, (1) imposing
849   an interface condition in addition to the standard Dirichlet and Neumann boundary conditions,
850   and (2) admitting discontinuities in fracture-normal fluid flux. The model is different from the
851   standard dual-porosity double-permeability model which requires the formulation of two
852   interacting mass conservation laws and the use of a smearing quantity called the 'shape factor'
853   resulting from domain separation and regularization. The initial conditions of the primary
854   unknowns are trivially set up as 0 since we are solving only for the changes.

855   The fluid diffusion in a fluid-saturated porous medium in the absence of fractures is governed by
856   a simplified version of equation (A1):

857
$$\left(\phi_{m0}(\underline{x})\left(C_m + C_\rho\right)\right)\dot{p}(\underline{x},t) + \nabla\cdot\underline{v}(\underline{x},t) = s(\underline{x},t), \quad \underline{x}\in\Omega \tag{A7}$$

858   **A.2 Seismic Source Parameters and Scaling Laws**

859   The key equations used in calculating the seismic source parameters are shown here. First, M_0
860   can be calculated from the fracture dimension and the recorded $\Delta\tau$. Depending on the fracture
861   geometry and the faulting regime, various formulas are available. Here, we opt for the one
862   suitable for a rectangular dip-slip fracture (Kanamori and Anderson, 1975):

863
$$M_0 = \frac{\pi(\lambda + 2\mu)}{4(\lambda + \mu)}\Delta\tau W^2 L \tag{A8}$$

864   where W is the fracture width (assumed as 1 m in the numerical examples under plane strain), λ
865   and μ are the Lame's constant and the shear modulus of the medium.

866   Second, M_w is calculated from M_0 following (Hanks & Boore, 1984):

867
$$Mw = \frac{2}{3}\left(\lg M_0 - 9.1\right) \tag{A9}$$

868 Finally, we adopt the following scaling laws that directly relate the permeability changes on a
869 fracture to the event magnitude (Ishibashi et al., 2016):

870
$$k_{\perp} / k = 116.4 \times 10^{0.46 Mw}$$
$$k_{//} / k = 13.1 \times 10^{0.46 Mw}$$
(A10)

871 where $k_{\perp}$ and $k_{//}$ are the fracture permeabilities orthogonal and parallel to the fracture, and k is a
872 reference permeability of the fracture prior to slip and is related to the fracture length via a power
873 scaling law. Other methods for mapping permeability changes from induced seismicity data are
874 available (e.g., Fang et al., 2018).

875 Because of the simple linear relation between $k_{\perp}$ and $k_{//}$, the normalized permeability changes
876 along the fracture-normal and -tangential directions, denoted as k_j^* where j = $\perp$ or $//$ and calculated
877 as $k_j^* = (k_j/k)-(k_j/k)_{min}/((k_j/k)_{max}-(k_j/k)_{min})$, are the same, therefore, both are collectively denoted
878 as k^*. This quantity is used in section 4.6.

879 A.3 Definition of Triggered and Induced Events

880 Some qualitative definitions of triggered and induced seismicity exist (e.g., McGarr & Simpson,
881 1997). Here we propose the following quantitative definition for distinguishing a triggered event
882 from an induced event based on the initial stress on a fracture in relation to the peak and residual
883 frictional strengths:

884
$$\sqrt{\left\|\boldsymbol{\sigma}_0 ' \cdot \underline{n}\right\|^2 - \left(\boldsymbol{\sigma}_0 ': \underline{n} \otimes \underline{n}\right)^2} \le \mu_d \left(\boldsymbol{\sigma}_0 ': \underline{n} \otimes \underline{n}\right), \quad induced$$
$$\mu_d \left(\boldsymbol{\sigma}_0 ': \underline{n} \otimes \underline{n}\right) < \sqrt{\left\|\boldsymbol{\sigma}_0 ' \cdot \underline{n}\right\|^2 - \left(\boldsymbol{\sigma}_0 ': \underline{n} \otimes \underline{n}\right)^2} \le \mu_s \left(\boldsymbol{\sigma}_0 ': \underline{n} \otimes \underline{n}\right), \quad triggered$$
(A11)

885 where $\boldsymbol{\sigma}_0'$, $\underline{n}$, μ_s and μ_d are the same as in the main text.

886 Equation (A11) states that from a loading point of view, the key difference between the two lies
887 in that an induced event represents shear failure on a fault that is otherwise tectonically inactive
888 with respect to the background stress state, whereas a triggered event is indicative of a fault that
889 is nevertheless expected to produce an earthquake given the background stress state but the
890 process towards failure is favorably accelerated. Our definition is consistent with the
891 aforementioned one. As a result, upon seismicity, a triggered event releases a substantial amount
892 of tectonic stress whereas an induced event releases mostly anthropogenic stress.

893 A.4 Poroelastic Stress Invariants

894 The two poroelastic stress invariants are calculated according to standard formulations except for
895 the use of the effective poroelatic stress tensor $\boldsymbol{\sigma}_p'$. Under plane strain, they read:

896
$$\frac{1}{3}I_1' = \frac{1}{3}(1+v)\left(\sigma'_{px} + \sigma'_{py}\right)$$
(A12)

897
$$\sqrt{J_2{}'} = \sqrt{\frac{1}{6}\left[\left(\sigma'_{px}-\sigma'_{py}\right)^2 + \left(\sigma'_{py}-\nu\left(\sigma'_{px}+\sigma'_{py}\right)\right)^2 + \left(\sigma'_{px}-\nu\left(\sigma'_{px}+\sigma'_{py}\right)\right)^2\right]} + \left(\sigma'_{pxy}\right)^2 \qquad (A13)$$

898 where ν is the Poisson's ratio, σ'_{px} and σ'_{py} are the two normal components and σ'_{pxy} is the shear
899 component of $\mathbf{\sigma}_p{}'$.

900 Using these two stress invariants, we define an *excess poroelastic shear stress invariant* denoted as
901 *MC*, which reads:

902
$$MC = \sqrt{J_2{}'} - \sin(\phi)\frac{1}{3}I_1{}' \qquad (A14)$$

903 Here,

904
$$\phi = \tan^{-1}(\mu_s) \qquad (A15)$$

905 Equation (A14) is adapted from the invariant form of the Mohr Coulomb yield function (e.g.,
906 Borja, 2013) by setting the cohesion to 0 and the Lode's angle as $\pi/6$. In a sense, *MC* is the invariant
907 form of *CFF*.

908 For case 3, equations (A12) and (A13) are used to calculate $I_1'/3$, $\sqrt{J_2'}$ and $\sqrt{J_2'}$-$sin(\phi)I_1'/3$ shown
909 in Figure 7. For cases 1 and 2 devoid of the coupling effect, substituting equation (12) into
910 equations (A12) and (A13) yields the following equivalent poroelastic stress invariants (the
911 continuous instead of the discrete fluid pressure is used here):

912
$$\frac{1}{3}I_1{}' = -\frac{2}{3}(1+\nu)\alpha p \qquad (A16)$$

913
$$\sqrt{J_2{}'} = 0 \qquad (A17)$$

914 Given the parameters used in this study, specifically, $\nu = 0.25$, $a = 0.8$ and $\mu_s = 0.6$, equation (A16)
915 predicts that $I_1'/3 \approx -0.67p$ and $\sqrt{J_2'}$-$sin(\phi)I_1'/3 \approx 0.34p$ for cases 1 and 2.

916 **A.5 Associating Seismicity With The *LSDF***

917 In section 4.2.2, we have pointed out that in cases 2 and 3, a positive correlation between the
918 distance and the origin time can be observed for an explicit event occurring along the *LSDF*
919 (Figure 3a) but not for an implicit event in the hosting rock (Figure 3b). Here in Figures A1b and
920 A1c, we single out the explicit events in cases 2 and 3 and plot them in the *R-T* space, and the
921 color indicates the index *I* of a fracture (equation (8)) with which an explicit event is associated.
922 For case 1, an explicit event cannot be defined; nonetheless, the events on fractures at the same
923 locations (Figure 3d) are plotted and colored with the same *I* for comparison (Figure A1a). In
924 Figures A1b andA1c, the progressive development of events along a deterministic fracture

925 becomes evident, i.e., events of the same color delineate a parabolic trend. However, this cannot
926 be observed in Figure A1a.

927
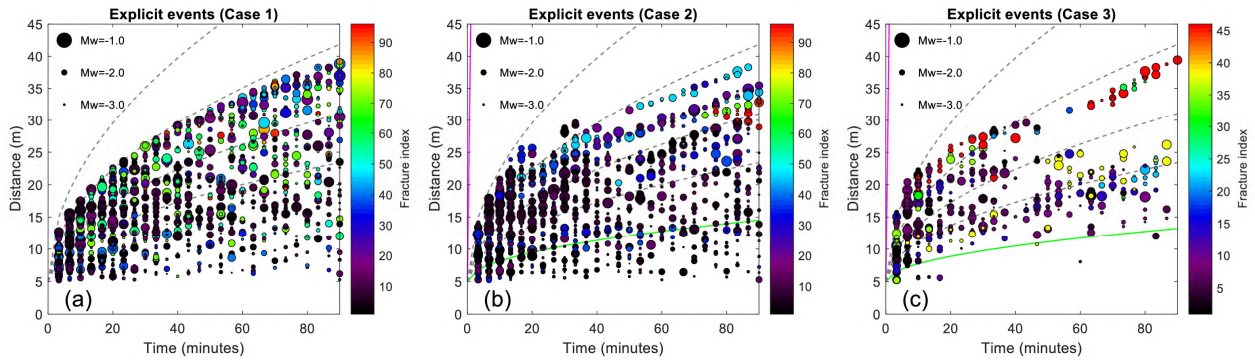
Figure A1. *R-T* plot of the explicit seismic events colored with the associated fracture index *I*. (a) Case 1, (b) case 2 and
929 (c) case 3. Notice that the notion of an explicit event only applied to cases 2 and 3. Nonetheless, for case 1, the events at
930 the same locations are plotted for comparison.

A.6 Effect of The Parameter *r*

932 In section 4.5.1, we have showed the distribution of $\Delta\tau$ in relation to M_w and L, which does not
933 vary much among the three cases. The parameter *r* in equation (18) is generated following a
934 uniform distribution in all cases. Here, to show the effect of *r*, we run a case otherwise identical
935 to case 3 except for the removal of *r* and the result is shown in Figure A2. While the model
936 produces the same ranges of M_w and L, $\Delta\tau$ is concentrated right above 1 MPa. This is not typically
937 observed in real data, implying that $\Delta\tau$ mostly does not reach the maximum likely stress drop.

938
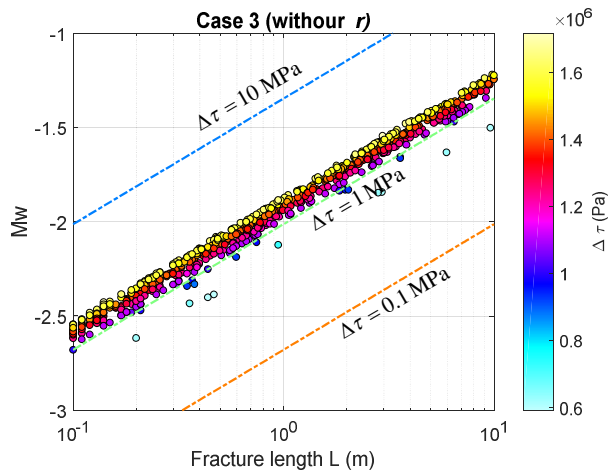
Figure A2. The distribution of $\Delta\tau$ in the M_w-L space for case 3 without considering the random parameter *r* in equation
940 (18).

Reference

Altmann, J. B., Müller, B. I. R., Müller, T. M., Heidbach, O., Tingay, M. R. P., & Weißhardt, A. (2014). Pore pressure stress coupling in 3D and consequences for reservoir stress states and fracture reactivation. *Geothermics*, 52, 195-205.

Andrews, D. J. (1976). Rupture velocity of plane strain shear cracks. *Journal of Geophysical Research*, *81*(32), 5679-5687.

Bachmann, C. E., Wiemer, S., Goertz-Allmann, B. P., & Woessner, J. (2012). Influence of pore-pressure on the event-size distribution of induced earthquakes. *Geophysical Research Letters*, *39*(9).

Baisch, S., & Harjes, H. P. (2003). A model for fluid-injection-induced seismicity at the KTB, Germany. *Geophysical Journal International*, *152*(1), 160-170.

Baisch, S., Vörös, R., Rothert, E., Stang, H., Jung, R., & Schellschmidt, R. (2010). A numerical model for fluid injection induced seismicity at Soultz-sous-Forêts. *International Journal of Rock Mechanics and Mining Sciences*, 47(3), 405-413.

Barbour, A. J., Norbeck, J. H., & Rubinstein, J. L. (2017). The effects of varying injection rates in Osage County, Oklahoma, on the 2016 M w 5.8 Pawnee earthquake. *Seismological Research Letters*, *88*(4), 1040-1053.

Berkowitz, B. (2002). Characterizing flow and transport in fractured geological media: A review. *Advances in Water Resources*, 25(8), 861-884.

Biot, M. A. (1941). General theory of three-dimensional consolidation. *Journal of applied physics*, *12*(2), 155-164.

Block, L. V., Wood, C. K., Yeck, W. L., & King, V. M. (2015). Induced seismicity constraints on subsurface geological structure, Paradox Valley, Colorado. *Geophysical Journal International*, *200*(2), 1172-1195.

Bonnet, E., Bour, O., Odling, N. E., Davy, P., Main, I., Cowie, P., & Berkowitz, B. (2001). Scaling of fracture systems in geological media. *Reviews of geophysics*, *39*(3), 347-383.

Borja, R. I. (2013). *Plasticity: modeling & computation*. Berlin: Springer.

Bruel, D. (2007). Using the migration of the induced seismicity as a constraint for fractured hot dry rock reservoir modelling. *International Journal of Rock Mechanics and Mining Sciences*, *44*(8), 1106-1117.

Byerlee, J. (1978). Friction of rocks. In *Rock friction and earthquake prediction* (pp. 615-626). Basel: Birkhäuser.

Carcione, J. M., Currenti, G., Johann, L., & Shapiro, S. (2018). Modeling fluid injection induced microseismicity in shales. *Journal of Geophysics and Engineering*, *15*(1), 234.

Carcione, J. M., Da Col, F., Currenti, G., & Cantucci, B. (2015). Modeling techniques to study CO2-injection induced micro-seismicity. *International Journal of Greenhouse Gas Control*, *42*, 246-257.

Chang, K. W., & Segall, P. (2016a). Injection-induced seismicity on basement fractures including poroelastic stressing. *Journal of Geophysical Research: Solid Earth*, 121(4), 2708-2726.

Chang, K. W., & Segall, P. (2016b). Seismicity on basement fractures induced by simultaneous fluid injection–extraction. *Pure and Applied Geophysics*, *173*(8), 2621-2636.

Chang, K. W., & Segall, P. (2017). Reduction of Injection-Induced Pore-Pressure and Stress in Basement Rocks Due to Basal Sealing Layers. *Pure and Applied Geophysics*, 174(7), 2649-2661.

Deichmann, N., Kraft, T., & Evans, K. F. (2014). Identification of fractures activated during the stimulation of the Basel geothermal project from cluster analysis and focal mechanisms of the larger magnitude events. *Geothermics*, *52*, 84-97.

Deng, K., Liu, Y., & Harrington, R. M. (2016). Poroelastic stress triggering of the December 2013 Crooked Lake, Alberta, induced seismicity sequence. *Geophysical Research Letters*, 43(16), 8482-8491.

Duverger, C., Godano, M., Bernard, P., Lyon‐Caen, H., & Lambotte, S. (2015). The 2003–2004 seismic swarm in the western Corinth rift: Evidence for a multiscale pore pressure diffusion process along a permeable fracture system. *Geophysical Research Letters*, 42(18), 7374-7382.

983 Fan, Z., Eichhubl, P., & Gale, J. F. (2016). Geomechanical analysis of fluid injection and seismic fracture slip for the
984   Mw4. 8 Timpson, Texas, earthquake sequence. *Journal of Geophysical Research: Solid Earth*, 121(4), 2798-2812.

985 Fang, Y., Elsworth, D., & Cladouhos, T. T. (2018). Reservoir permeability mapping using microearthquake
986   data. *Geothermics*, *72*, 83-100.

987 Farmahini-Farahani, M., & Ghassemi, A. (2016). Simulation of micro-seismicity in response to injection/production in
988   large-scale fracture networks using the fast multipole displacement discontinuity method (FMDDM). *Engineering
989   Analysis with Boundary Elements*, *71*, 179-189.

990 Goertz-Allmann, B. P., & Wiemer, S. (2012). Geomechanical modeling of induced seismicity source parameters and
991   implications for seismic hazard assessment. *Geophysics*, *78*(1), KS25-KS39.

992 Goertz-Allmann, B. P., Goertz, A., & Wiemer, S. (2011). Stress drop variations of induced earthquakes at the Basel
993   geothermal site. *Geophysical Research Letters*, *38*(9).

994 Gutenberg, B. (1956). The energy of earthquakes. *Quarterly Journal of the Geological Society*, *112*(1-4), 1-14.

995 Hanks, T. C., & Boore, D. M. (1984). Moment-magnitude relations in theory and practice. *Journal of Geophysical Research:
996   Solid Earth*, *89*(B7), 6229-6235.

997 Hardebol, N. J., Maier, C., Nick, H., Geiger, S., Bertotti, G., & Boro, H. (2015). Multiscale fracture network
998   characterization and impact on flow: A case study on the Latemar carbonate platform. *Journal of Geophysical
999   Research: Solid Earth*, 120(12), 8197-8222.

1000 Hirata, T. (1989). A correlation between the b value and the fractal dimension of earthquakes. *Journal of Geophysical
1001   Research: Solid Earth*, *94*(B6), 7507-7514.

1002 Hirthe, E. M., & Graf, T. (2015). Fracture network optimization for simulating 2D variable-density flow and
1003   transport. *Advances in Water Resources*, 83, 364-375.

1004 Hummel, N., & Shapiro, S. A. (2012). Microseismic estimates of hydraulic diffusivity in case of non-linear fluid-rock
1005   interaction. *Geophysical Journal International*, *188*(3), 1441-1453.

1006 Hummel, N., & Shapiro, S. A. (2013). Nonlinear diffusion-based interpretation of induced microseismicity: A Barnett
1007   Shale hydraulic fracturing case study. *Geophysics*, *78*(5), B211-B226.

1008 Ishibashi, T., Watanabe, N., Asanuma, H., & Tsuchiya, N. (2016). Linking microearthquakes to fracture permeability
1009   change: The role of surface roughness. *Geophysical Research Letters*, *43*(14), 7486-7493.

1010 Izadi, G., & Elsworth, D. (2014). Reservoir stimulation and induced seismicity: Roles of fluid pressure and thermal
1011   transients on reactivated fractured networks. *Geothermics*, *51*, 368-379.

1012 Jin, L., & Zoback, M. D. (2015a). An Analytical Solution for Depletion-induced Principal Stress Rotations In 3D and its
1013   Implications for Fracture Stability. In *AGU Fall Meeting Abstracts*.

1014 Jin, L., & Zoback, M. D. (2015b). Identification of fracture-controlled damage zones in microseismic data–an example
1015   from the Haynesville shale. *SEG Technical Program Expanded Abstracts 2015*, 726-730.

1016 Jin, L., & Zoback, M. D. (2016a). Including a stochastic discrete fracture network into one-way coupled poromechanical
1017   modeling of injection-induced shear re-activation. In *50th US Rock Mechanics/Geomechanics Symposium*. American
1018   Rock Mechanics Association.

1019 Jin, L., & Zoback, M. D. (2016b). Impact of Poro-Elastic Coupling and Stress Shadowing on Injection-Induced
1020   Microseismicity in Reservoirs Embedded With Discrete Fracture Networks. In *AAPG Annual Convention and
1021   Exhibition*.

1022 Jin, L., & Zoback, M. D. (2017). Fully Coupled Nonlinear Fluid Flow and Poroelasticity in Arbitrarily Fractured Porous
1023   Media: A Hybrid-Dimensional Computational Model. *Journal of Geophysical Research: Solid Earth*, *122*(10), 7626-
1024   7658.

1025 Jin, L., & Zoback, M. D. (2018a). Modeling Induced Seismicity: Co-Seismic Fully Dynamic Spontaneous Rupture
1026   Considering Fault Poroelastic Stress. In *52nd US Rock Mechanics/Geomechanics Symposium*. American Rock
1027   Mechanics Association.

Jin, L., & Zoback, M. D. (2018b). Fully Dynamic Spontaneous Rupture Due to Quasi-Static Pore Pressure and Poroelastic Effects: An Implicit Nonlinear Computational Model of Fluid-Induced Seismic Events. *Journal of Geophysical Research: Solid Earth,* 123. https://doi.org/10.1029/2018JB015669

Johann, L., Dinske, C., & Shapiro, S. A. (2016). Scaling of seismicity induced by nonlinear fluid-rock interaction after an injection stop. *Journal of Geophysical Research: Solid Earth*, *121*(11), 8154-8174.

Johri, M., Zoback, M. D., & Hennings, P. (2014). A scaling law to characterize fracture-damage zones at reservoir depthsFracture Damage Zones at Depth. *AAPG Bulletin*, *98*(10), 2057-2079.

Kanamori, H., & Anderson, D. L. (1975). Theoretical basis of some empirical relations in seismology. *Bulletin of the seismological society of America*, *65*(5), 1073-1095.

Keranen, K.M. & Weingarten, M. (2018). Induced Seismicity. *Annual Review of Earth and Planetary Sciences*. 46, 149-174.

Ma, X., & Zoback, M. D. (2017). Laboratory experiments simulating poroelastic stress changes associated with depletion and injection in low-porosity sedimentary rocks. *Journal of Geophysical Research: Solid Earth*, *122*(4), 2478-2503.

Maillot, B., Nielsen, S., & Main, I. (1999). Numerical simulation of seismicity due to fluid injection in a brittle poroelastic medium. *Geophysical Journal International*, 139(2), 263-272.

McGarr, Arthur F. and Simpson, David (1997). A broad look at induced and triggered seismicity. *In: Rockbrust and seismicity in mines* (pp. 385-396). Rotterdam: Balkema.

Megies, T., & Wassermann, J. (2014). Microseismicity observed at a non-pressure-stimulated geothermal power plant. *Geothermics*, 52, 36-49.

Moriya, H., Niitsuma, H., & Baria, R. (2003). Multiplet-clustering analysis reveals structural details within the seismic cloud at the Soultz geothermal field, France. *Bulletin of the Seismological Society of America*, *93*(4), 1606-1620.

Mukuhira, Y., Asanuma, H., Niitsuma, H., & Häring, M. O. (2013). Characteristics of large-magnitude microseismic events recorded during and after stimulation of a geothermal reservoir at Basel, Switzerland. *Geothermics*, *45*, 1-17.

Mukuhira, Y., Dinske, C., Asanuma, H., Ito, T., & Häring, M. O. (2017). Pore pressure behavior at the shut-in phase and causality of large induced seismicity at Basel, Switzerland. *Journal of Geophysical Research: Solid Earth*, *122*(1), 411-435.

Murphy, S., O'Brien, G. S., McCloskey, J., Bean, C. J., & Nalbant, S. (2013). Modelling fluid induced seismicity on a nearby active fracture. *Geophysical Journal International*, 194(3), 1613-1624.

Okubo, P. G., & Aki, K. (1987). Fractal geometry in the San Andreas fracture system. *Journal of Geophysical Research: Solid Earth*, *92*(B1), 345-355.

Poupinet, G., Ellsworth, W. L., & Frechet, J. (1984). Monitoring velocity variations in the crust using earthquake doublets: An application to the Calaveras Fracture, California. *Journal of Geophysical Research: Solid Earth*, *89*(B7), 5719-5731.

Raziperchikolaee, S., Alvarado, V., & Yin, S. (2014). Microscale modeling of fluid flow-geomechanics-seismicity: Relationship between permeability and seismic source response in deformed rock joints. *Journal of Geophysical Research: Solid Earth*, 119(9), 6958-6975.

Riffracture, J., Dempsey, D., Archer, R., Kelkar, S., & Karra, S. (2016). Understanding Poroelastic Stressing and Induced Seismicity with a Stochastic/Deterministic Model: an Application to an EGS Stimulation at Paralana, South Australia, 2011. *In Proc. 41st Stanford Workshop on Geothermal Reservoir Engineering*, SGP-TR-209.

Rothert, E., & Shapiro, S. A. (2007). Statistics of fracture strength and fluid-induced microseismicity. *Journal of Geophysical Research: Solid Earth*, *112*(B4).

Safari, R., & Ghassemi, A. (2016). Three-dimensional poroelastic modeling of injection induced permeability enhancement and microseismicity. *International Journal of Rock Mechanics and Mining Sciences*, *84*, 47-58.

Schoenball, M., Davatzes, N. C., & Glen, J. M. (2015). Differentiating induced and natural seismicity using space-time-magnitude statistics applied to the Coso Geothermal field. *Geophysical Research Letters*, *42*(15), 6221-6228.

1072 Scuderi, M. M., & Collettini, C. (2016). The role of fluid pressure in induced vs. triggered seismicity: Insights from rock
1073   deformation experiments on carbonates. *Scientific reports*, *6*, 24852.

1074 Segall, P. (1985). Stress and subsidence resulting from subsurface fluid withdrawal in the epicentral region of the 1983
1075   Coalinga earthquake. *Journal of Geophysical Research: Solid Earth*, *90*(B8), 6801-6816.

1076 Segall, P., & Fitzgerald, S. D. (1998). A note on induced stress changes in hydrocarbon and geothermal
1077   reservoirs. *Tectonophysics*, *289*(1), 117-128.

1078 Segall, P., & Lu, S. (2015). Injection-induced seismicity: Poroelastic and earthquake nucleation effects. *Journal of
1079   Geophysical Research: Solid Earth*, *120*(7), 5082-5103.

1080 Segall, P., Grasso, J. R., & Mossop, A. (1994). Poroelastic stressing and induced seismicity near the Lacq gas field,
1081   southwestern France. *Journal of Geophysical Research: Solid Earth*, *99*(B8), 15423-15438.

1082 Shapiro, S. A., Huenges, E., & Borm, G. (1997). Estimating the crust permeability from fluid-injection-induced seismic
1083   emission at the KTB site. *Geophysical Journal International*, *131*(2).

1084 Shapiro, S. A., Rentsch, S., & Rothert, E. (2005). Characterization of hydraulic properties of rocks using probability of
1085   fluid-induced microearthquakes. *Geophysics*, *70*(2), F27-F33.

1086 Shapiro, S. A., Rothert, E., Rath, V., & Rindschwentner, J. (2002). Characterization of fluid transport properties of
1087   reservoirs using induced microseismicity. *Geophysics*, *67*(1), 212-220.

1088 Shi, Y., & Bolt, B. A. (1982). The standard error of the magnitude-frequency b value. *Bulletin of the Seismological Society
1089   of America*, *72*(5), 1677-1687.

1090 Stabile, T. A., Giocoli, A., Perrone, A., Piscitelli, S., & Lapenna, V. (2014). Fluid injection induced seismicity reveals a
1091   NE dipping fracture in the southeastern sector of the High Agri Valley (southern Italy). *Geophysical Research
1092   Letters*, *41*(16), 5847-5854.

1093 Stark, M. A., & Davis, S. D. (1996). Remotely triggered microearthquakes at The Geysers geothermal field,
1094   California. *Geophysical research letters*, *23*(9), 945-948.

1095 Tarrahi, M., & Jafarpour, B. (2012). Inference of permeability distribution from injection-induced discrete microseismic
1096   events with kernel density estimation and ensemble Kalman filter. *Water Resources Research*, *48*(10).

1097 Terakawa, T. (2014). Evolution of pore fluid pressures in a stimulated geothermal reservoir inferred from earthquake
1098   focal mechanisms. *Geophysical Research Letters*, *41*(21), 7468-7476.

1099 Terakawa, T., Miller, S. A., & Deichmann, N. (2012). High fluid pressure and triggered earthquakes in the enhanced
1100   geothermal system in Basel, Switzerland. *Journal of Geophysical Research: Solid Earth*, *117*(B7).

1101 Terzaghi, Karl (1936). Relation Between Soil Mechanics and Foundation Engineering: Presidential Address. *Proceedings,
1102   First International Conference on Soil Mechanics and Foundation Engineering, Boston*. 3, 13-18.

1103 Verdon, J. P., Stork, A. L., Bissell, R. C., Bond, C. E., & Werner, M. J. (2015). Simulation of seismic events induced by
1104   CO2 injection at In Salah, Algeria. *Earth and Planetary Science Letters*, *426*, 118-129.

1105 Vermylen, J., & Zoback, M. D. (2011, January). Hydraulic fracturing, microseismic magnitudes, and stress evolution in
1106   the Barnett Shale, Texas, USA. In *SPE Hydraulic Fracturing Technology Conference*. Society of Petroleum Engineers.

1107 Vujević, K., Graf, T., Simmons, C. T., & Werner, A. D. (2014). Impact of fracture network geometry on free convective
1108   flow patterns. *Advances in Water Resources*, *71*, 65-80.

1109 Waldhauser, F., & Ellsworth, W. L. (2002). Fracture structure and mechanics of the Hayward fracture, California, from
1110   double-difference earthquake locations. *Journal of Geophysical Research: Solid Earth*, *107*(B3).

1111 Wassing, B. B. T., Van Wees, J. D., & Fokker, P. A. (2014). Coupled continuum modeling of fracture reactivation and
1112   induced seismicity during enhanced geothermal operations. *Geothermics*, *52*, 153-164.

1113 Yeck, W. L., Weingarten, M., Benz, H. M., McNamara, D. E., Bergman, E. A., Herrmann, R. B., ... & Earle, P. S. (2016).
1114   Far-field pressurization likely caused one of the largest injection induced earthquakes by reactivating a large
1115   preexisting basement fracture structure. *Geophysical Research Letters*, *43*(19).

1116   Yoon, J. S., Zang, A., & Stephansson, O. (2014). Numerical investigation on optimized stimulation of intact and
1117   naturally fractured deep geothermal reservoirs using hydro-mechanical coupled discrete particles joints model.
1118   *Geothermics*, 52, 165-184.

1119   Zbinden, D., Rinaldi, A. P., Urpi, L., & Wiemer, S. (2017). On the physics-based processes behind production-induced
1120   seismicity in natural gas fields. *Journal of Geophysical Research: Solid Earth*, 122(5), 3792-3812.

1121   Zhao, X., & Paul Young, R. (2011). Numerical modeling of seismicity induced by fluid injection in naturally fractured
1122   reservoirs. *Geophysics*, 76(6), WC167-WC180.

1123   Zoback, M. D., & Zinke, J. C. (2002). Production-induced normal fractureing in the Valhall and Ekofisk oil fields. *In The
1124   Mechanism of Induced Seismicity* (pp. 403-420). Basel: Birkhäuser.